Tropical Cyclone Data Assimilation with Coyote Uncrewed Aircraft System Observations, Very Frequent Cycling, and a New Online Quality Control Technique

ALTUG AKSOY,[a,b] JOSEPH J. CIONE,[b] BRITTANY A. DAHL,[a,b] AND PAUL D. REASOR[b]

[a] *Cooperative Institute for Marine and Atmospheric Studies, University of Miami, Miami, Florida*
[b] *Hurricane Research Division, NOAA/Atlantic Oceanographic and Meteorological Laboratory, Miami, Florida*

(Manuscript received 21 May 2021, in final form 16 November 2021)

ABSTRACT: A unique dataset obtained from the Coyote small uncrewed aircraft system (sUAS) in the inner-core boundary layer of Hurricane Maria (2017) is assimilated using NOAA's Hurricane Ensemble Data Assimilation System (HEDAS) for data assimilation and Hurricane Weather Research and Forecasting (HWRF) system for model advances. The case of study is 1800 UTC 23 September 2017 when Maria was a category-3 hurricane. In addition to the Coyote observations, measurements collected by the NOAA Lockheed WP-3D Orion and U.S. Air Force C-130 aircraft were also included. To support the assimilation of this unique dataset, a new online quality control (QC) technique in HEDAS scales the observation–background difference by the total uncertainty during data assimilation and uses the interquartile range outlier method to identify outlier observations. Experimental setup includes various very frequent cycling scenarios for a control that does not assimilate Coyote observations, assimilation of Coyote observations in addition to the control observations, and the application of online QC. Findings suggest progressively improved analyses with more-frequent cycling, Coyote assimilation, and application of online QC. This applies to verification statistics computed at the locations of both Coyote and non-Coyote observations. In terms of the storm structure, only experiments that assimilated the Coyote observations were able to reproduce the double-eyewall structure that was observed at the time of the analysis, which is more consistent with the intensity of the storm according to the observations that were collected. Limitations of the study and future plans are also discussed.

SIGNIFICANCE STATEMENT: Findings from this study illustrate the significant impact difficult-to-obtain, near-surface observations can have on improving the accuracy of tropical cyclone structure and intensity. Adding these novel measurements in a way that also includes advanced cycling and quality control techniques in data assimilation has the potential to improve public forecasts that are reliant upon detailed depictions of storm strength and boundary layer structure prior to landfall. The results speak to the importance of parallel and consistent advancements in modeling, data assimilation, and observational capabilities to improve the depiction of the tropical cyclone inner-core structure in numerical models.

KEYWORDS: Boundary layer; Hurricanes/typhoons; Aircraft observations; Data quality control; In situ atmospheric observations; Filtering techniques; Kalman filters; Numerical analysis/modeling; Quality assurance/control; Data assimilation

1. Introduction

Hurricanes are complex atmospheric phenomena that have proven to be challenging to predict. While substantial progress has been made in the prediction of their track over the last two decades, improvements in hurricane intensity forecasting have been slower (e.g., National Hurricane Center 2017). One complexity that renders intensification of hurricanes difficult to forecast is the multiscale nature of the processes involved, from the synoptic in the hurricane steering environment down to turbulent and microphysical scales in the inner core (e.g., Rogers et al. 2013). In the present study, the focus is on observing capabilities in the hurricane inner core to improve the representation of the vortex structure in analyses.

The hurricane inner core is a notoriously difficult region to observe, both remotely and in situ. Interpretation of remote satellite brightness temperature measurements is challenging due to the complexity of the microphysical processes involved under the typically convective atmospheric conditions (Zhang et al. 2016), while in situ sampling by reconnaissance aircraft is rare and hazardous, especially at low altitudes within the planetary boundary layer (PBL) due to the existence of large ocean waves, convective downdrafts, and sea spray (Cione et al. 2016). Uncrewed aircraft systems (UAS) therefore offer the unique capability to provide observations in these undersampled regions and thereby improve hurricane forecasts through utilization of such observations in data assimilation (DA).

Although UAS observations in the hurricane PBL are critically important, the small-scale nature of the turbulent processes they potentially sample brings about complexities in DA and modeling applications. Indeed, the rapid increase in computational resources worldwide in recent years has brought about an equally fast-paced advance in operational modeling capabilities (Bauer et al. 2015; Yano et al. 2018) down to horizontal resolutions in the range of 1–10 km. This is known as the "gray zone," where clouds and convective transport are partly resolved and it becomes unclear whether parameterization of deep convection is necessary (Tomassini et al. 2017). Several DA techniques have been proposed to address the challenges of such highly nonlinear regimes within the context of ensemble-based (Houtekamer and Zhang

Corresponding author: Altug Aksoy, aaksoy@rsmas.miami.edu

DOI: 10.1175/MWR-D-21-0124.1

2016), variational (Bannister 2017), as well as particle-filter (Van Leeuwen et al. 2019) applications.

While great emphasis is being given to developing or improving data assimilation methods to deal with the increasingly nonlinear nature of observation–background differences (also called innovations), the equally important question of how to treat observational errors in these regimes seems to draw not as much attention. Understandably, the diversity and complexity of modern observing platforms prompts developers of DA techniques to increasingly rely on data providers to ensure the quality of their data. There may also be an assumption that existing online quality control (QC) methods will continue to be suitable if incoming data are already of good quality. Online QC here is defined as a QC procedure that is applied in addition to the traditional QC step, which occurs during the preprocessing of observations, and takes advantage of the knowledge of model background information during assimilation, hence the term "online."

Indeed, online QC methods have been proposed and implemented since the early applications of DA methods. For instance, as early as 1991, QC is given great emphasis, and it is acknowledged that "the accuracy of the forecast is usually good enough to be very useful in detecting uncharacteristically larger errors in the observations" (National Research Council 1991). More than a decade later, Auligné and McNally (2007) suggest that, in an adaptive bias correction scheme, the population of observations that pass QC ultimately determines how bias is calculated, thus potentially leading to a feedback between bias correction and QC. They argue that the use of the mode, rather than the mean, of first-guess innovations should be influenced less by nonhomogeneous populations (such as a mixture of clear-sky and cloudy radiances in their case) and thus better suited to reduce feedback. They then propose a "pseudo-mode," where observations are assigned smaller weights in the calculation of bias as their first-guess departures increase. A similar approach is adopted in Sakov and Sandery (2017), but this time applying a scalable magnification factor to the observation error itself to reduce its impact with increasing innovation magnitude. However, increasing model resolution toward the "gray zone" mentioned above introduces further complications as models begin to resolve atmospheric phenomena at multiple spatial and temporal scales in the convective to synoptic range. In such circumstances, QC becomes much more challenging because observations that may appear representative of the mesoscale or convective scale could have a higher likelihood of getting filtered out as outliers at the synoptic scale.

The current article approaches observational QC in the context of tropical cyclone (TC) inner-core DA. A case is chosen with a unique combination of observations, including not only those that are typically available from reconnaissance aircraft (Rogers et al. 2013) and atmospheric motion vector (AMV) wind retrievals (Velden et al. 2005) but also data collected by the Coyote, a small UAS (sUAS) platform (Cione et al. 2016, 2020) that samples the lower altitudes of the PBL. This combination of observations offers a unique dataset, sampling distinct regions in and around the TC inner core at varying temporal and spatial resolutions. It will be demonstrated that a revisit to QC in a holistic manner that is consistent with how DA is performed may result in improved analyses.

The DA system employed is the Hurricane Ensemble Data Assimilation System (HEDAS), the performance of which was successfully evaluated in various applications spanning assimilation of reconnaissance aircraft observations (Aksoy et al. 2013; Aberson et al. 2015), Global Hawk (Braun et al. 2013) uncrewed aircraft system (UAS) observations (Christophersen et al. 2018a), and satellite observations (Christophersen et al. 2018b). It uses a square root ensemble Kalman filter (Whitaker and Hamill 2002) and is coupled with the numerical model component of NOAA's Hurricane Weather Research and Forecasting (HWRF) system (Bernardet et al. 2015).

The article is structured as follows. Section 2 describes the online QC methodology and section 3 provides the details of the experimental setup. Results are presented separately in observation space (section 4) and model space (section 5). Finally, a summary and further discussion is provided in section 6.

2. The online QC methodology

a. General description

A twofold approach to online observation QC is proposed. The first step involves elimination of observations that are deemed "erroneous" during the preprocessing stage. At this phase, no model background information is available and QC mostly relies on the expertise of data providers to distinguish "good" observations from "bad" observations. In many cases, data are provided along with quality classifications that can be utilized to decide which observations should pass QC during preprocessing. In some situations, observations are accompanied by observation error estimates that can be utilized to reduce the impact of observations with larger errors during DA. Once observations pass preprocessing, they become available for DA, at which time the model background information is also accessible. It is therefore possible to perform a direct comparison between the background and observations by interpolation from model space to observation space, thus making online QC feasible.

b. Schematic

The proposed online QC can be explained in five distinct steps (Fig. 1):

1) The observation y^0 is assumed to have passed QC during preprocessing and to be ready for assimilation. Its error (uncertainty) is prescribed by a Gaussian probability distribution with standard deviation σ^0.
2) During DA, the model background is also available, interpolated from model space to observation space at the observation's location. It is denoted y^b with a known error of σ^b also assumed to be the standard deviation of a Gaussian probability distribution.
3) The observation–background difference, $\Delta y = y^0 - y^b$, is also known as the innovation and it represents new information introduced by the observation.

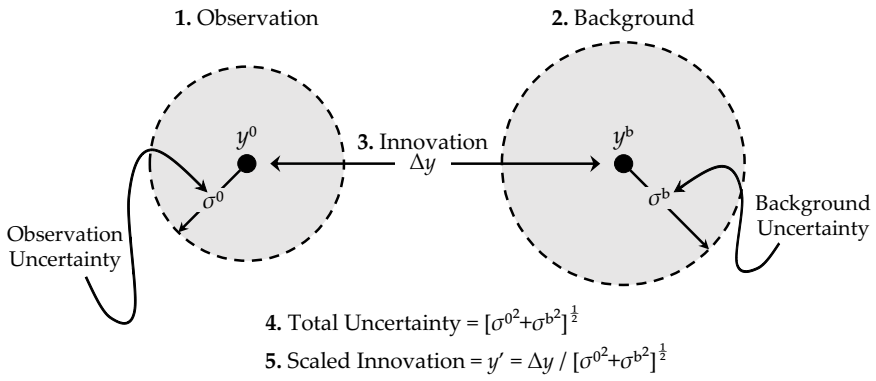

FIG. 1. Schematic of the main components of the online QC technique. (Note that the graphic is generated for visual convenience and only represents the case of large innovations.)

4) As the observation and background errors are assumed to be Gaussian, the innovation also has a Gaussian probability distribution with the total uncertainty of $(\sigma^{0^2} + \sigma^{b^2})^{1/2}$.
5) The total uncertainty can be used as a scaling factor to normalize the innovation to y'. In this manner, it is possible to pool all observations into a single population for the purposes of online QC.

c. *Technical details of online QC*

The availability of scaled innovations y' is an important advantage as it allows all observations to be considered in a single population for QC purposes. This is also necessary for practical purposes because observation numbers can vary significantly across observing platforms, especially for TC inner-core applications. For platforms that provide only a small number of observations, it may not be possible to perform robust QC analysis. The ability to combine all observations through normalization therefore makes it possible to include observations in the QC process regardless of the platform that provides them and their data volume compared to other platforms.

The purpose of the proposed online QC methodology is to detect outlier innovations in order to exclude their associated observations from assimilation and avoid strongly nonlinear DA updates. The one issue, however, is that even though the total uncertainty is assumed to follow a normal distribution, in practice this is often violated, especially at meso- and smaller scales. In particular, in the TC inner core, meso-, convective, and turbulent scales are strongly coupled and expected to generate non-Gaussian background distributions due to strong nonlinearities at these scales (Poterjoy and Zhang 2011). Therefore, the outlier detection needs to be sufficiently robust under such circumstances.

Various statistical methods are proposed for outlier detection, generally classified as either univariate versus multivariate or parametric versus nonparametric techniques (Ben-Gal 2010). The scaling of innovations to y' by the total uncertainty allows all observations to be considered at once in a univariate application. Among univariate parametric outlier detection methods, the interquartile range (IQR) is chosen due to its robustness in the face of the possibility of non-Gaussian probability distributions of y'. The IQR is defined as the difference between the 75th and 25th percentiles of a dataset:

$$\text{IQR} = Q_3 - Q_1, \tag{1}$$

where Q_n represents the nth quartile. In other words, Q_1 is the median of the lower half of a dataset, while Q_3 is the median of the upper half of a dataset. Outliers are then defined as samples that are outside the range

$$(Q_1 - 1.5 \times \text{IQR}; Q_3 + 1.5 \times \text{IQR}). \tag{2}$$

In descriptive statistics, the limits in Eq. (2) constitute the "whiskers" (also known as the "fences") of box-and-whisker diagrams (Tukey 1977). Being based on the population quartiles, they are, by definition, nonparametric, i.e., they represent properties of statistical populations without making any assumptions of the underlying statistical distributions. This makes the IQR-based outlier detection method attractive for data assimilation applications when it is not safe to assume Gaussianity in innovation populations.

3. Experimental setup

a. *TC case of interest*

The case of interest is Hurricane Maria as observed on 1800 UTC 23 September 2017. At this time, the TC was a category-3 hurricane, centered at 25.9°N latitude and 72.3°W longitude with a minimum sea level pressure (MSLP) of 952 hPa and intensity (maximum 10-m wind speed) of 100 kt (~51.4 m s^{-1}). For further details, refer to Pasch et al. (2018, 3–4).

b. *Data assimilation system*

In this study, the experimental data assimilation system HEDAS (Aksoy et al. 2012, 2013), developed at NOAA's Atlantic Oceanographic and Meteorological Laboratory (AOML) Hurricane Research Division (HRD), is utilized. HEDAS is based on an exact parallel implementation of the square root ensemble Kalman filter (EnKF) introduced by Whitaker and Hamill (2002). It is specifically designed to assimilate high-resolution TC inner-core observations. A unique aspect of

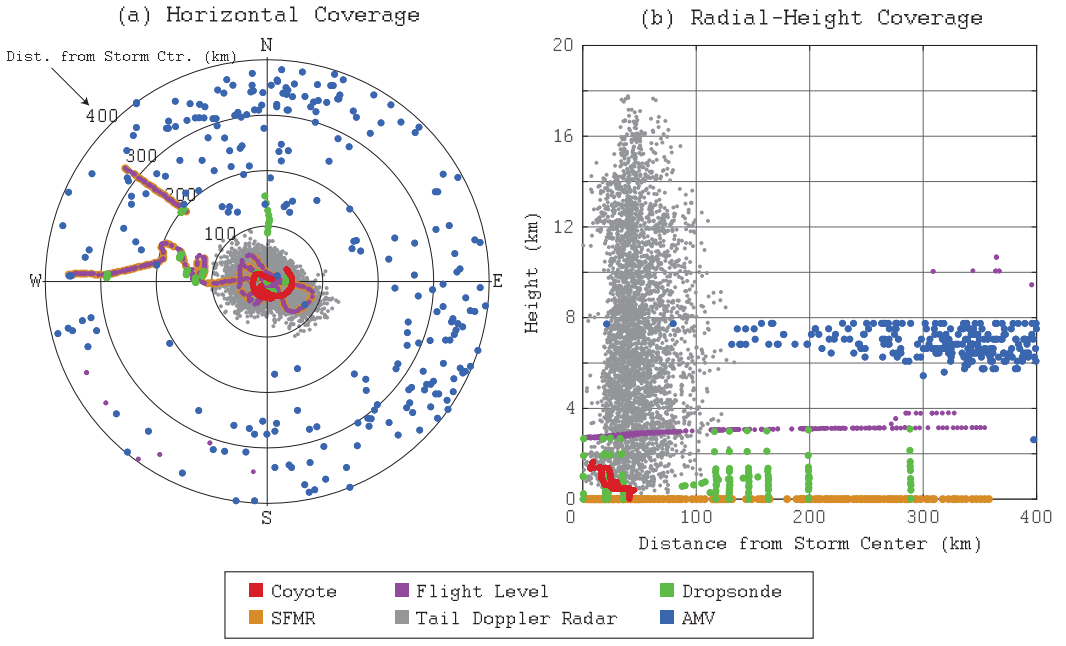

FIG. 2. Spatial coverage of kinematic observations within 400 km of the storm center: (a) horizontal coverage and (b) radial–height coverage. The platforms from which observations were obtained are indicated by the marker colors. All observations are storm centered, accounting for their horizontal position relative to the storm position interpolated at the time of measurement. (Note that some thinning is applied judiciously to enhance the visibility of observations from various platforms. For a comparison of the actual number of observations, refer to Table 1.)

HEDAS is its storm-relative observation processing capability (Aksoy 2013) that accounts for storm motion during assimilation cycles, allowing observations to be randomly distributed into arbitrarily short assimilation windows. For the present study, this capability allows DA experiments to be designed with assimilation windows as short as 5 min.

c. *Numerical model*

The numerical model is the model component of HWRF, which is NOAA's operational TC forecasting system. The publicly available version 4.0a of this model is used (Bernardet et al. 2015), which is based on the operational HWRF as of late 2018. The model configuration is very similar to what is used in operations, except for the lack of ocean coupling, an outer domain and a vortex-following inner domain with 9- and 3-km horizontal grid spacings, and 61 vertical levels. Additional details of the configurations are contained in Table 1 of Christophersen et al. (2017). It should be noted that, in this case, only the numerical model portion of HWRF is used here for spinup and cycle-to-cycle model advances. Observation preprocessing and data assimilation components are carried out under HEDAS.

d. *Observational data*

At the time window of interest (1800 UTC 23 September 2017 ± 3 h), the inner core of Hurricane Maria was sampled by the NOAA Lockheed WP-3D Orion (P-3) and U.S. Air Force C-130 (C-130) aircraft. The types of observations assimilated from the P-3 include Tail Doppler Radar (TDR) radial wind superobservations (superobs) as detailed in Aksoy et al. (2012), GPS dropsonde (Hock and Franklin 1999) data, aircraft flight-level wind and temperature observations, and Stepped Frequency Microwave Radiometer (SFMR) wind speed retrievals at 10-m altitude (Uhlhorn et al. 2007). Except for the TDR, the same instruments are also available on the C-130. Further details can be found in Table 3 of Aksoy et al. (2013). Additional, non-aircraft data include AMVs (Velden et al. 2005).

In addition to the routinely available observations described above, two Coyote sUAS missions were conducted by NOAA: flights 3 and 4 that were both eyewall missions, as described in Table 1 of Cione et al. (2020). These two consecutive flights together provided an almost complete azimuthal coverage of the eyewall, mostly below an altitude of 1.5 km. The observations collected by the Coyote include temperature, relative humidity, and atmospheric pressure. Instantaneous wind speed and direction are computed by vector subtraction of the true air velocity from the ground velocity. The details of the sensors and data processing can be found in Cione et al. (2016). Although the data acquisition rate for the Coyote is generally 1 Hz, no thinning or superobbing is applied to Coyote data in this study. This is mainly to maximize the Coyote data's impact on the HEDAS analyses, as it is the only platform that provides observations in the eyewall at these very low altitudes. Investigation of the impact of thinning will be the focus of future studies.

The spatial distribution of the observations used in this study is shown in Figs. 2 and 3. In terms of kinematic

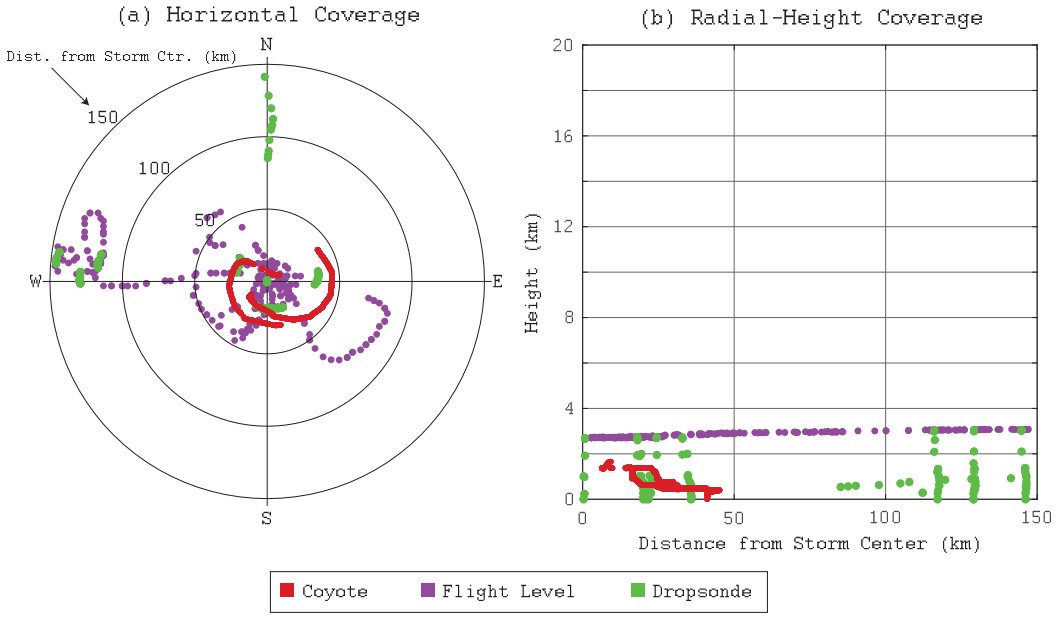

FIG. 3. As in Fig. 2, but for the spatial coverage of thermodynamic observations within 150 km of the storm center. Except for the dispersed coverage from three dropsonde soundings, no thermodynamic observations are available outside the shown radius of 150 km.

observations (Fig. 2), not only do the TDR superobs comprise the largest number of observations of all platforms assimilated, but they also provide the best spatial coverage in the inner core, especially at higher altitudes. In contrast, all other aircraft observing platforms (including the Coyote) provide observations only at and below the flight level (~3 km). Nevertheless, compared to the other platforms, sUAS observations sample a mostly data-void region near the surface within 50 km of the storm center. Compared to the kinematic observations, the spatial coverage of the thermodynamic observations (Fig. 3) is constrained to below the aircraft flight level of ~3 km. The total number of thermodynamic observations is also much smaller, as there exists no thermodynamic platform that complements the spatial coverage of the TDR.

The total number of observations that are available for assimilation is summarized in Table 1 (column heading "All"). Mostly due to the large number of TDR superobs, kinematic observations by far outweigh thermodynamic observations. But, when TDR superobs are not considered, observations from the Coyote comprise the majority of kinematic observations, especially near the TC inner core where AMVs are not a significant contribution (Fig. 2). This discrepancy is even more pronounced for thermodynamic observations: compared to the flight-level and dropsonde platforms, the

TABLE 1. Observing platforms and the number of observations that were assimilated and filtered out by online QC for each platform.

Observing platform	No. of observations		
	All[a]	Online QCd	Percent online QCd (%)
Kinematic observations			
TDR radial wind speed superobs	48 161	798	1.63
Coyote zonal and meridional wind speed	6016	736	10.90
AMV zonal and meridional wind speed	2159	0	0.00
Flight-level zonal and meridional wind speed	764	20	2.55
Dropsonde zonal and meridional wind speed	312	20	6.02
SFMR wind speed	258	6	2.33
Thermodynamic observations			
Coyote temperature	3008	69	2.29
Coyote specific humidity	3002	74	2.47
Flight-level temperature	345	12	3.48
Flight-level specific humidity	334	58	17.37
Dropsonde temperature	119	15	12.61
Dropsonde specific humidity	109	26	23.85

[a] "All" indicates observations assimilated without the application of online QC.

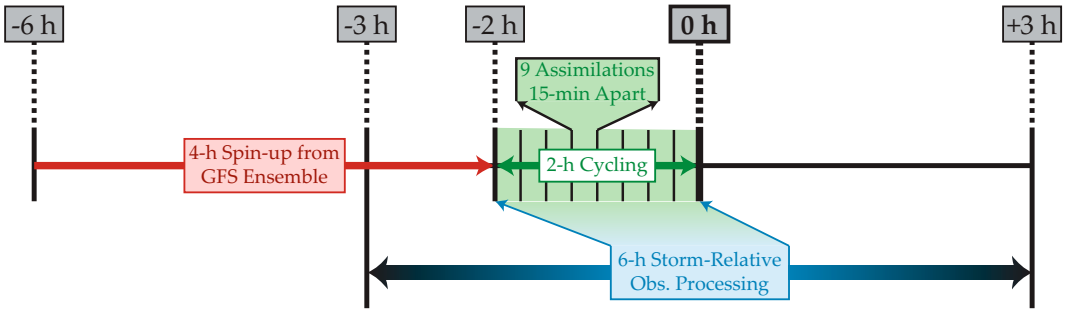

FIG. 4. Schematic of the default HEDAS spinup and cycling configuration. The final storm-scale analysis is valid at 0 h, when all observations available within the 6-h window have been assimilated.

measurements from the Coyote are greater in number by nearly one order of magnitude.

e. *Experimental setup*

HEDAS is a "cold-start" ensemble system that uses a global ensemble as its initial condition and only performs high-resolution cycling of TC inner-core observations within a 6-h period. Almost all experiments in the present study share a common initial ensemble that is obtained by the 4-h spinup from the first 30 ensemble members of NOAA's Global Forecast System (GFS) analysis ensemble valid at 1200 UTC (one additional experiment employs a 5-h spinup). The various experiments only differ in the types of observations assimilated, number of assimilation cycles performed, and whether online QC is applied. The storm-relative observation processing capability mentioned before (Aksoy 2013) allows all available 6-h observations to be distributed into any desired number of assimilation windows. But in each case, the final high-resolution cycle occurs at 1800 UTC 23 September 2017. The default HEDAS cycling setup is demonstrated in Fig. 4.

The experiments follow a three-tiered approach (Table 2). First, a "Control" experiment is designed where the standard set of observations are assimilated without the Coyote. In this scenario, observations are equally distributed into nine assimilation cycles 15 min apart between 1600 and 1800 UTC. In Tier A, the default HEDAS configuration is only modified for cycling strategy. In two experiments, cycles are shortened to 10 and 5 min, resulting in 13 and 25 assimilation cycles, respectively. In a fourth experiment, ensemble spinup is carried out for 5 h followed by thirteen 5-min assimilation cycles. In Tier B, these four cycling strategies are repeated by also assimilating the Coyote observations. In Tier C, online QC is also applied. In this manner, a total of 12 experiments are carried out to explore the combined impacts of cycling strategy, Coyote observations, and online QC.

4. Results in observation space

In the present study, the focus is on the incremental impact of assimilating Coyote observations and applying online QC on the final, high-resolution, vortex-scale analyses in various cycling-strategy scenarios. Here, the investigation is conducted in observation space by comparing analyses directly to observations.

a. *Definitions of observation-space diagnostics*

Observation-space diagnostics are carried out following the general innovation-based methodology laid out in Aksoy et al. (2009). Recall that, for a given observation i, the innovation is defined as the observation-minus-forecast difference, $\Delta y_i^b = y_i^0 - y_i^b$. The mean innovation Δy^b is then the average of all innovations for a given observation type:

$$\Delta y^b = \frac{1}{M}\sum_{i=1}^{M} \Delta y_i^b, \tag{3}$$

where the summation is taken over all M observations of a particular type. Assuming that observations themselves are not biased, the presence of significant mean innovation could indicate biases in both the model and data assimilation system.

The second diagnostic of interest is the root-mean-square (rms) innovation, computed using the deviations of the innovations from the mean:

$$r^b = \sqrt{\frac{1}{M}\sum_{i=1}^{M}\left(\Delta y_i^b - \Delta y^b\right)^2}\,. \tag{4}$$

TABLE 2. Summary of the experiments carried out.

	Exp. 1	Exp. 2	Exp. 3	Exp. 4
Tier A: Control	9 × 15-min cycles[a]	13 × 10-min cycles	25 × 5-min cycles	13 × 5-min cycles
Tier B: Coyote	Tier A + Coyote	Tier A + Coyote	Tier A + Coyote	Tier A + Coyote
Tier C: online QC	Tier B + online QC	Tier B + online QC	Tier B + online QC	Tier B + online QC

[a] Default HEDAS configuration.

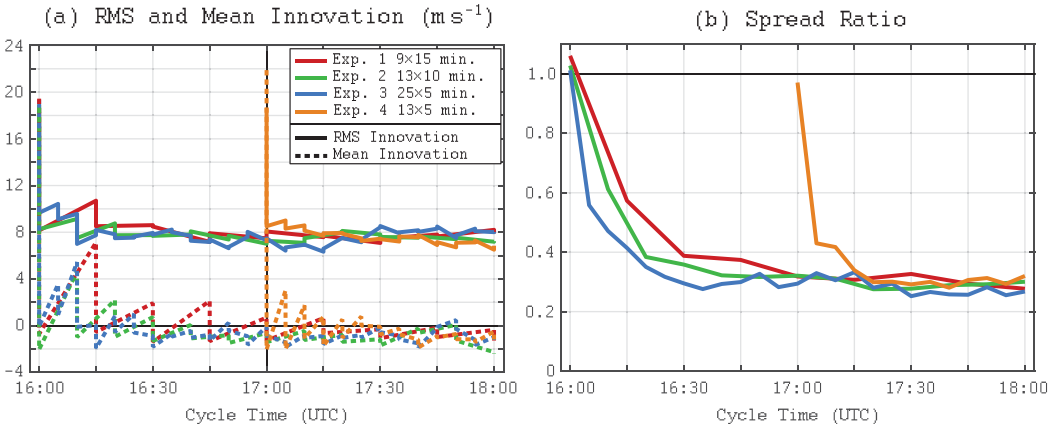

FIG. 5. Coyote horizontal wind observation-space diagnostics for the control (Tier A) experiments, as a function of time: (a) RMS (solid) and mean (dashed) innovations, and (b) spread ratio. Colors indicate various cycling strategies (Exp. 1–4).

The reason for removing the mean innovation is to ensure that the rms innovation is the best approximation for the random error of the innovations.

The third and final diagnostic measures the adequacy of ensemble spread by comparing it to the "optimal" ensemble spread. The domain-averaged standard deviation of ensemble-member innovations, denoted as ensemble spread, is calculated as follows:

$$s^b = \sqrt{\frac{1}{M}\sum_{i=1}^{M}\left[\frac{1}{N-1}\sum_{j=1}^{N}\left(\Delta_i y_j^b - \Delta_i y^b\right)^2\right]}, \tag{5}$$

where N represents ensemble size, and thus the inner summation is to obtain ensemble variance at the location of the ith observation. This leads to the definition of the spread ratio R that measures how adequate the actual ensemble spread s^b is compared to the "optimal" ensemble spread (one that adequately represents the statistics of forecast error):

$$R = \frac{s^b}{\sqrt{r^{b2} - \sigma_0^2}}, \tag{6}$$

where σ_0^2 is the average observation error variance of a particular observation type.

It should be noted briefly that the overarching motivation behind exploring these observation-space diagnostics in a cycling data assimilation system is to expose and reduce the model and data-assimilation biases while also maintaining a healthy random variability among the ensemble members that results in a near-optimal spread ratio. Indeed, the goal is not to seek near-zero rms innovations as is the case for mean innovations, as doing so would inevitably lead to the assimilation system giving more weight to the model background than the observations and result in filter divergence (e.g., Aksoy et al. 2012).

b. Observation-space diagnostics for Coyote observations

First, observation-space diagnostics for the Coyote observations are presented. This serves as an independent assessment for the control experiments because the Coyote observations are not assimilated. As explained in Table 2, diagnostics will be evaluated in three tiers. For each tier, the impact of the four different cycling strategies will be compared.

1) TIER A: CONTROL EXPERIMENTS

Figures 5–7 summarize the time evolution of the three innovation-based diagnostics for the Coyote horizontal wind (zonal and meridional combined), temperature, and specific humidity, respectively. For all of the wind diagnostics (Fig. 5), little difference can be discerned among the various cycling strategies for RMS innovation, which is reduced from the initial ~20 to ~8 m s^{-1} within a few cycles but remains at that level thereon. Mean innovation, on the other hand, is reduced significantly from ~20 m s^{-1} to slightly below zero but again does not vary much among the cycling experiments. But, nevertheless, the assimilation of a significant number of nearby TDR superobs likely helps in reducing the wind bias at these locations. Finally, spread ratio quickly drops to near 0.3 in all four runs, which indicates substantial underdispersion of ensemble spread. Even without the assimilation of Coyote observations at these locations, it is hypothesized that the large number of TDR superobs assimilated contributes to this outcome. Further optimization through thinning and/or superobbing may help reduce such underdispersion, but this is beyond the scope of the current study, as such an effort would require a larger sample of cases with varying density and spatial coverage of observations.

For the Coyote temperature (Fig. 6) and specific humidity (Fig. 7) observations, the results are different than their wind counterpart. Specifically, cycling strategy has a discernable impact on mean innovation, where more-frequent cycling appears to reduce the negative bias by ~0.3 K for temperature and ~0.4 g kg^{-1} for specific humidity on average. Since the processes that control temperature and moisture occur at smaller spatial and temporal scales due to stronger influence from convection, higher-frequency cycling that limits error growth in-between cycles (e.g., He et al. 2020) is believed to

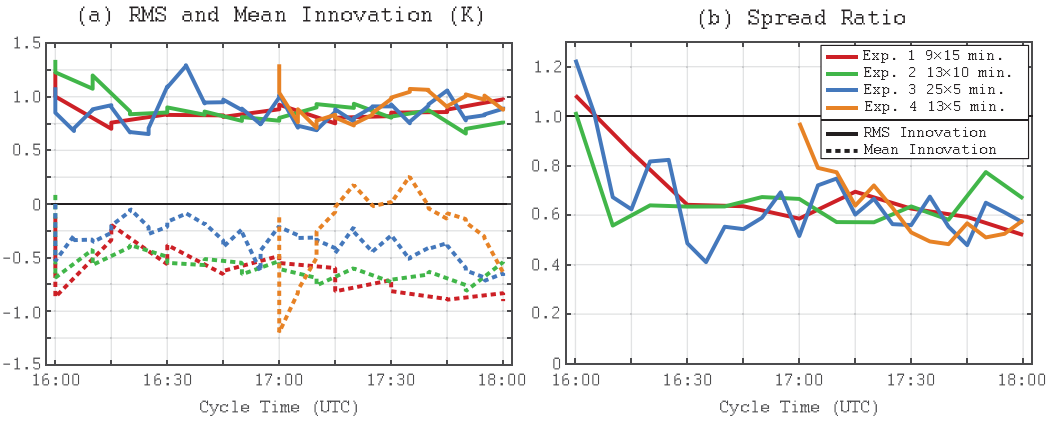

FIG. 6. As in Fig. 5, but for Coyote temperature observation-space diagnostics.

have a more positive impact on these fields. As for spread ratio, although there appears to be greater variability among the four experiments compared to the wind observations, there nevertheless does not appear to be a clear systematic difference among them in an average sense. This is because, regardless of cycling strategy, the same total number of observations are assimilated by the end of cycling, which results in similar cumulative behavior in ensemble spread evolution among these cycling strategies.

The statistics discussed above can be further compacted into average statistics calculated for the entirety of respective cycling periods. This is also a more practical approach with a large number of experiments and the many types of observed variables. Based on this cycle-averaging approach, experiment-to-experiment improvements are calculated for RMS error, absolute bias, total error (RMS error plus absolute bias), and spread ratio. For the first three diagnostics, improvement is indicated by tendency toward zero, while for spread ratio, improvement is indicated by tendency toward one.

These statistics are shown in Fig. 8, where the incremental improvements in various cycling strategies over the Control cycling setup are shown in rows 1–3. As was discussed in the context of Fig. 5, for Coyote wind observations, only small improvements in error (0–1 m s^{-1}) are obtained by varying the cycling strategy, although in Exp. 3, bias and total error are nevertheless improved by ~40% and ~15%, respectively. In contrast, cycle-averaged improvements at the locations of Coyote thermodynamic observations are much more pronounced. In both Exps. 3 and 4, greater reduction in bias and total error is observed both magnitude-wise and in a relative sense. In fact, except for row 4 (improvements from assimilating Coyote observations, to be discussed later), these experiments result in the largest improvements in bias and total error magnitude for both of the thermodynamic observation types.

2) TIER B: COYOTE ASSIMILATION EXPERIMENTS

The second tier of experiments assimilates the Coyote observations in addition to the Control observations and repeats the four cycling strategies investigated in the previous section. The incremental impact of assimilating the Coyote observations on the Control cycling setup is shown in row 4 of Fig. 8. For all three types of Coyote observations, assimilating

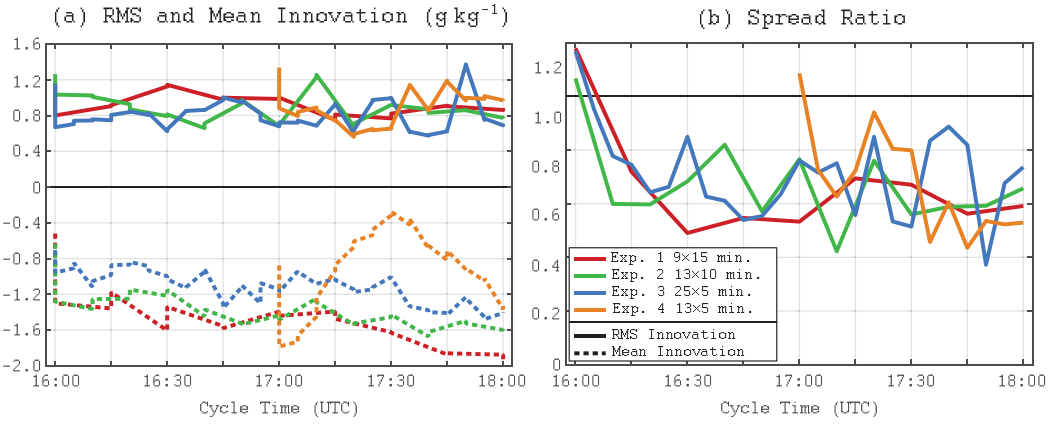

FIG. 7. As in Fig. 5, but for Coyote specific humidity observation-space diagnostics.

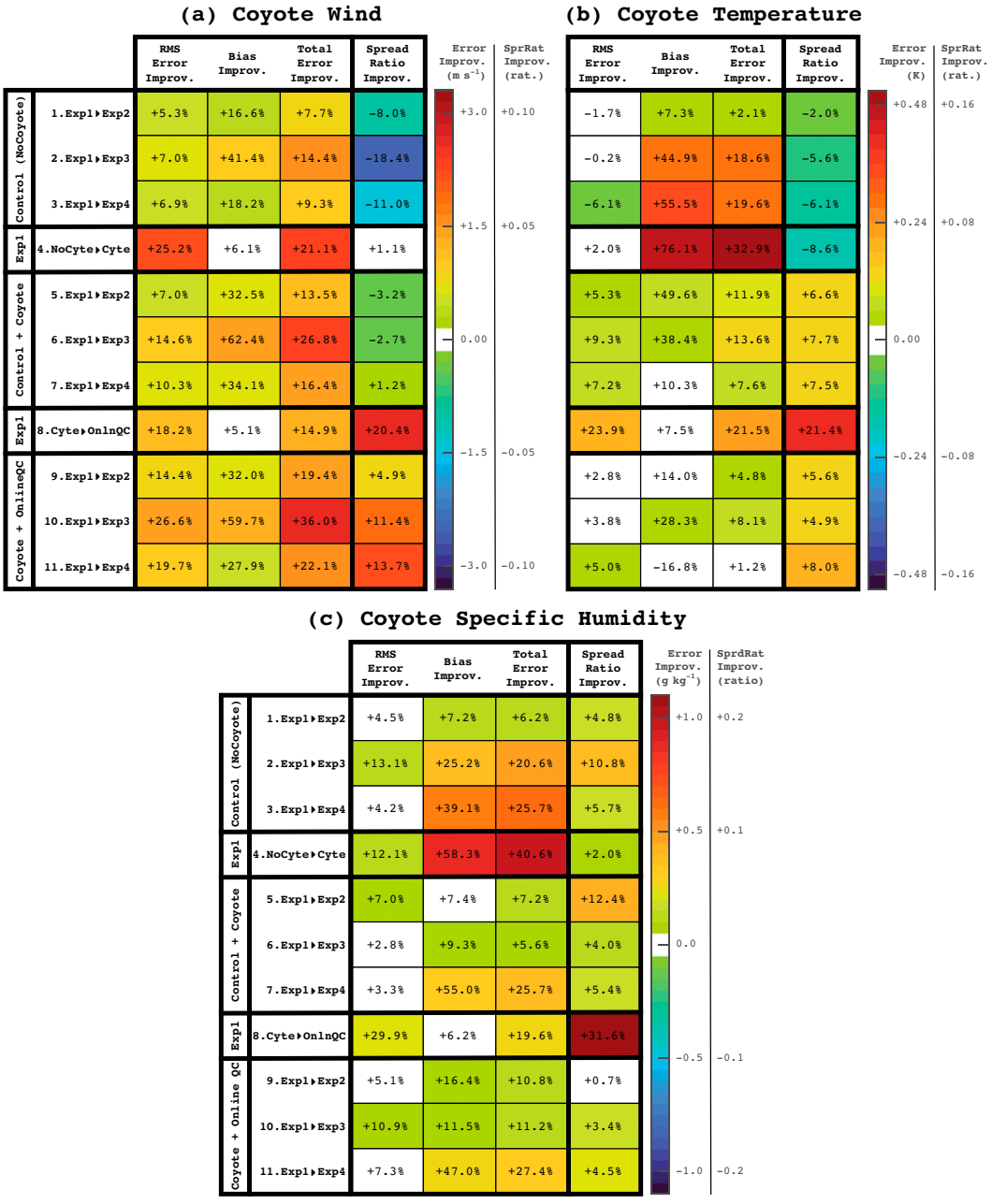

FIG. 8. Average incremental improvement in observation-space diagnostics, calculated at the locations of Coyote observations over all assimilation cycles. Pairs of experiments for which improvements are calculated are shown in each row, with the arrow indicating the direction in which improvement is calculated (negative numbers indicate degradation). Experiments 1–4 refer to the four different cycling strategies (Table 2). Various observation-space diagnostics are shown in columns. The magnitude-wise change for a given diagnostic is indicated by the color scale and the corresponding percent change is printed in the respective cell.

them results in the reduction in error. For wind, the impact of the Coyote observations is mostly on rms innovations, as bias was already reduced to near zero in the Control setup. For the thermodynamic observations, the reduction in error, especially in bias, is comparatively (percent-wise) much greater compared to wind. This is likely because there are very few other thermodynamic observations near the Coyote observation locations (Fig. 3). Therefore, assimilating Coyote thermodynamic observations allows them to influence the analysis to a much greater degree.

Experimentation with more-frequent cycling (rows 5–7 of Fig. 8) results in further improvements in error statistics. For

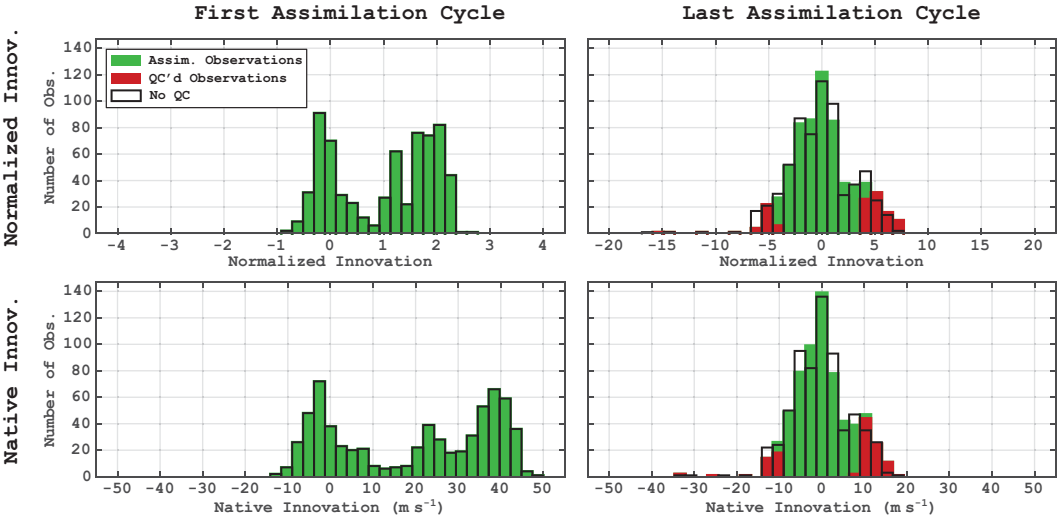

FIG. 9. Histograms of Coyote wind innovations in cycling experiment Exp. 1 (9 × 15-min cycles). (left) The first assimilation cycle and (right) the last assimilation cycle. (top) The distribution of normalized innovations and (bottom) the corresponding distributions of native innovations. Number of assimilated observations are shown in green bars while the numbers filtered out by online QC are shown in red bars. Distributions from the corresponding experiment that did not apply online QC (Control + Coyote) are shown in black-contoured bars.

Coyote wind observations, the greatest improvement is nearly by 27% (~3 m s^{-1}) in total error in Exp. 3 (25 × 5-min cycles). This suggests that further optimization (in this case through higher-frequency cycling) is needed to further counterbalance the indirect influence of the large number of nearby TDR superobs. Comparatively, improvements in temperature and moisture are smaller (indicated by the lighter shades of red and smaller percentages). It follows that just assimilating the Coyote observations (Fig. 8, row 4) dominates the relative improvements for the thermodynamic observations and the additional increases in cycling frequency therefore only bring about modest further improvements. This is an important finding that emphasizes the importance of directly observing the thermodynamic characteristics of the PBL. In the absence of such observations, it appears that other means, such as more-frequent cycling, are necessary to improve the thermodynamic representation of the PBL. But, when direct observations are available, such reliance on indirect "engineering" solutions is not as critical.

Finally, in terms of the spread ratio, the percent-wise changes are generally small. The spread ratio for all three types of Coyote observations is already below optimal, and the further changes brought about by the assimilation of the Coyote observations are in the range of only 5%–10%.

3) TIER C: ONLINE QC EXPERIMENTS

The focus is now turned to applying the online QC technique during assimilation. These results are summarized in the rows 8–11 of Fig. 8. The incremental impact of online QC in the Control cycling setup (row 8) is positive for all Coyote variables. This is not surprising because online QC filters out some of the higher innovations from assimilation, which has the direct impact of reducing the innovations Δy_i^b in the mean and rms innovation calculations, following Eqs. (3) and (4), thus leading to improvements in these metrics. The reduced rms innovation r^b also reduces the denominator of the spread ratio [Eq. (6)], effectively resulting in the overall increase in spread ratios in column 4. Experimentation with cycling strategy (rows 9–11) further improves all of the statistics.

The greatest relative (percent) impact is seen for Exp. 3, although in absolute terms the improvements for wind are much greater than temperature and moisture (indicated by the darker red cells in row 10, Figs. 8a–c, especially for total error). As discussed before, Coyote wind observations "compete" with a large number of TDR superobs in their vicinity. It is therefore conceivable that further optimization through cycling strategy helps improve their impact on DA. As for the Coyote thermodynamic observations, since they are almost the only source of information in the inner-core PBL, the greatest impact actually occurs simply from assimilating them (row 4, Figs. 8b,c), and further improvements through alteration of the cycling strategy and online QC are relatively smaller (rows 8–11, Figs. 8b,c).

Histograms of innovations are also explored to investigate how online QC interprets outliers and how it evolves through cycling. In Fig. 9, histograms of Coyote wind innovations are shown for the first and last cycles in default cycling (Exp. 1). In the first cycle, no observations are filtered out by online QC because of the bimodal probability distribution of wind innovations for which the online QC methodology is not able to identify outliers. This outcome is actually desirable because large updates to the background are needed at this time to account for the severity of both position and intensity errors. By the last assimilation cycle, almost all of these systematic errors are corrected in the background vortex, thus resulting

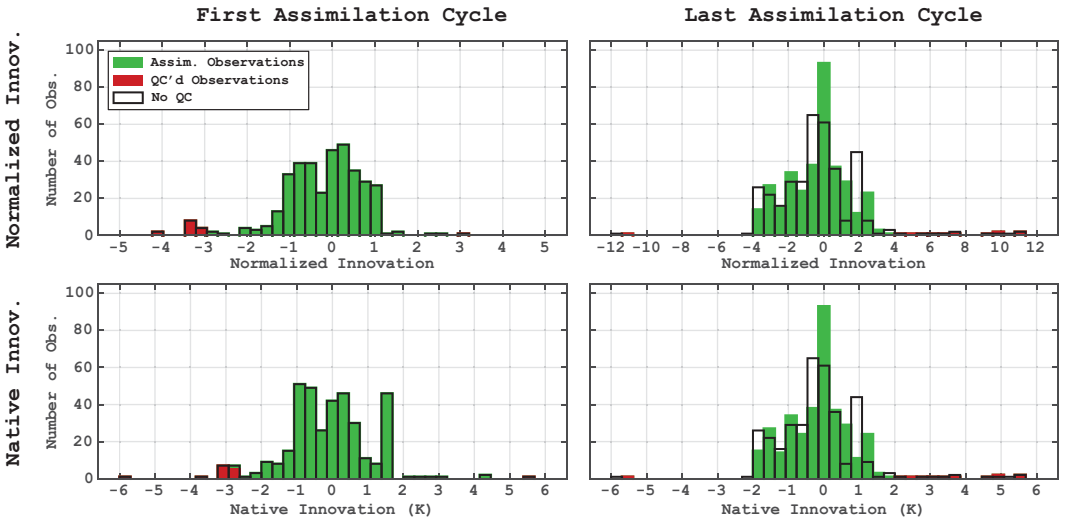

FIG. 10. As in Fig. 9, but for the Coyote temperature innovations.

in a probability distribution that is more akin to Gaussian, albeit with long tails and some skewness. This allows the online QC to be much more effective in capturing the tail ends of the innovation distribution as outliers and filtering them out.

It is also worthwhile to note some of the differences between Coyote assimilation experiments with and without online QC. Comparing the two probability distributions, i.e., the green and red bars together with online QC versus the black bars without online QC, flatter tails and a sharper peak in the background probability distribution are obtained when online QC is applied, suggesting that there is a cumulative positive effect of online QC through the assimilation cycles.

Looking further at Coyote temperature (Fig. 10) and specific humidity (Fig. 11) distributions, the important difference from the Coyote wind distributions is that, while the peak of the distributions is shifted toward zero, even at the final assimilation cycle, their width remains generally similar. This confirms the previous finding that the improvements in the thermodynamic observations are mostly in bias, while rms innovation remains high. But of note also is that, with online QC, the histograms have more pronounced peaks around the median. This is a desired outcome because, in EnKF applications, background innovation PDFs are assumed to be of Gaussian nature. It appears that the application of online QC significantly improves the quality of the analyses in this regard, as evidenced by the difference in the last-cycle background distributions with online QC (green histograms) versus without (black-contoured histograms).

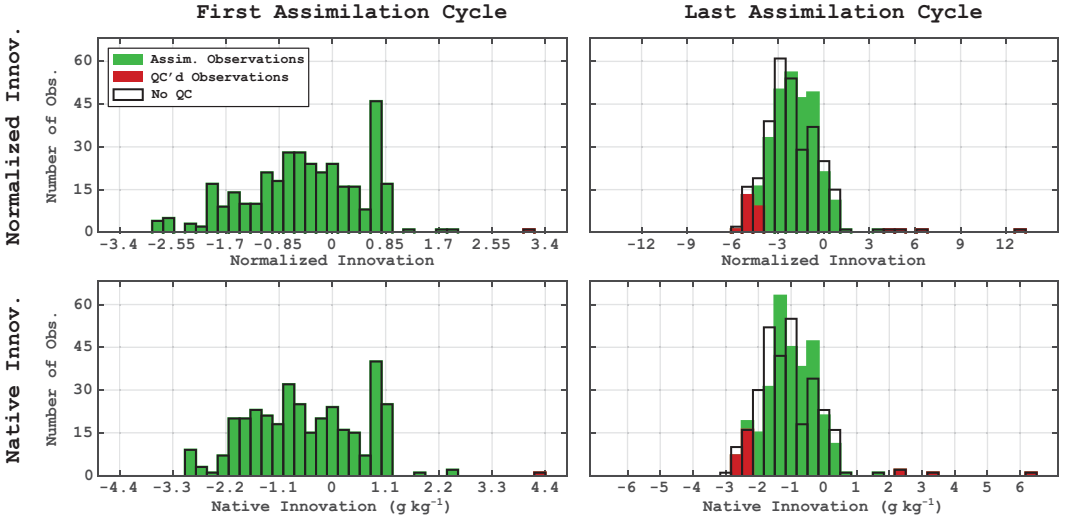

FIG. 11. As in Fig. 9, but for the Coyote specific humidity innovations.

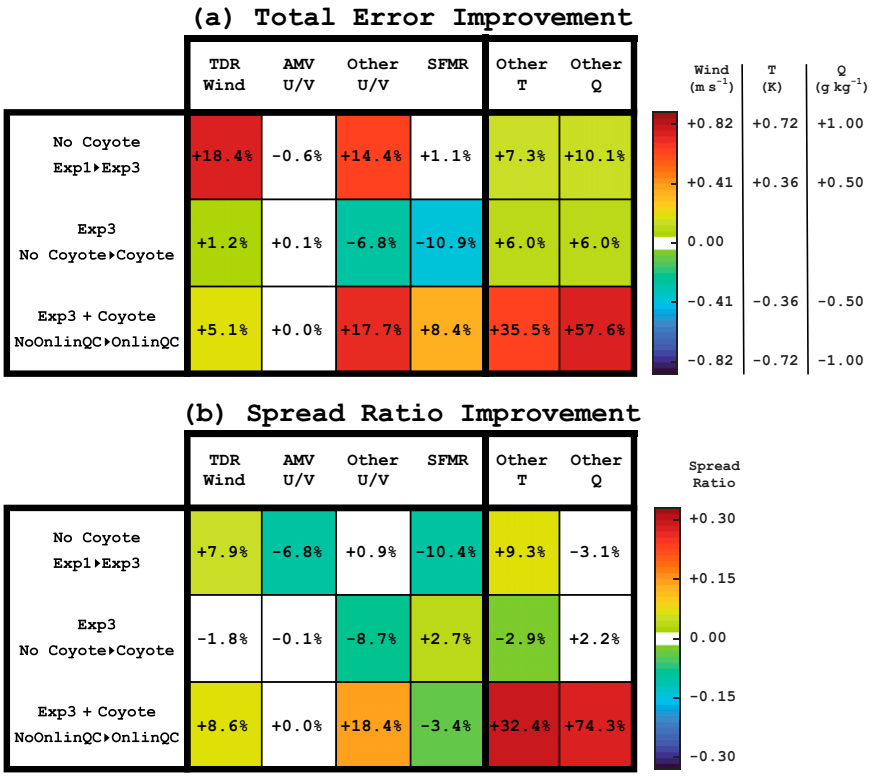

FIG. 12. Average incremental improvement for observation-space diagnostics calculated over all assimilation cycles at the locations of non-Coyote observations, where "Other" refers to the combined flight-level and dropsonde platforms: (a) improvements in the total error and (b) improvements in the spread ratio. Pairs of experiments for which improvements are calculated are shown in each row, with the arrow indicating the direction in which improvement is calculated (negative numbers indicate degradation). Only improvements for cycling experiment Exp. 3 (25 × 5-min cycles) are shown. The magnitude change for a given statistic is indicated by the color scale and the corresponding percent change is printed in the respective cell.

c. Observation-space diagnostics for non-Coyote observations

The discussion is now broadened to non-Coyote observations. As these observations are assimilated regardless of whether Coyote observations are also assimilated, their locations serve as an independent measure of the impact of Coyote observations. Figure 12 summarizes the improvements in total error and spread ratio calculated at the locations of non-Coyote observation types. The focus is now solely on the Exp. 3 cycling strategy (25 × 5-min cycles), as it was previously found to result in the greatest improvements in Coyote observations. Incremental improvements are calculated in three tiers as before: Exp. 1 (default) to Exp. 3 cycling strategy with no Coyote observations, the incremental impact of Coyote observations in Exp. 3, the further incremental impact of online QC in Exp. 3 with Coyote observations, and finally the combined overall impact of Exp. 3 cycling strategy, Coyote observations, and online QC on Control with the default cycling strategy.

1) TIER A: CONTROL EXPERIMENT WITH HIGH-FREQUENCY CYCLING

As shown in Table 1, there are five types of non-Coyote wind observations: TDR superobs, SFMR wind speed, flight-level and dropsonde wind, and AMVs. Due to their similar vertical and horizontal coverage (Figs. 2 and 3), hereon, flight-level and dropsonde observations are included in one group as "Other" observations. The improvements in total error at the locations of these wind observations are shown in columns 1–4 of Fig. 12a. The more-frequent cycling strategy of Exp. 3 introduces large improvements for TDR superobs and Other-wind observations, while practically resulting in none for AMV and SFMR platforms. For AMVs, this is likely due to their distance to the inner core both radially and vertically (Fig. 2), where smaller departures from observed wind combined with the slower evolution of the dynamics at outer radii do not necessitate very frequent cycling. For SFMR observations, it is believed that the preexisting tuning in their observation error leads to variability as a function of rain rate (Aksoy et al. 2013) and thus their assimilation does not appear to necessitate further optimization through cycling strategy.

Shifting focus to the non-Coyote thermodynamic observations, there are only two types in the dataset: flight-level and dropsonde (Table 1). Employing the same reasoning as before, these observations are grouped together as "Other" and the improvements in total error are shown in columns

5–6 of Fig. 12a. For both temperature and specific humidity, the more-frequent cycling strategy of Exp. 3 results in small improvements in total error magnitude. Furthermore, unlike the Coyote thermodynamic observations for which improvements were mostly in bias (Figs. 8b,c, row 2), the improvements for the non-Coyote observations are mostly in rms innovation (not shown). One contributing factor is that, at this point between Exp. 1 and Exp. 3, Coyote observations are still not assimilated but non-Coyote observations always are. Therefore, the assimilation of the non-Coyote thermodynamic observations in Exp. 1 has likely already improved bias. This is admittedly a hypothesis that could be tested through further experimentation, but is beyond the scope of the current study.

In terms of spread ratio (Fig. 12b), generally small overall impact is observed for all observation types both in absolute and relative terms. This is similar to what was observed for the Coyote observations themselves (Figs. 5–7), as the average spread ratio is mostly controlled by the total number of observations assimilated, which varies very little by cycling strategy.

2) TIER B: HIGH-FREQUENCY CYCLING WITH COYOTE OBSERVATIONS

When Coyote observations are also assimilated employing the cycling strategy of Exp. 3 (Fig. 12, row 2), except for SFMR, only small impacts can be seen on the total error in wind observations. For the SFMR observations, the relatively large degradation by ~0.4 m s^{-1} (~11%) suggests that the corrections to the low-level wind field introduced by the Coyote observations compete with those from the SFMR observations in a way that is slightly detrimental from the perspective of how well the analysis fits the SFMR observations. This may partially be due to the fact that SFMR wind speed observations are remotely retrieved by an instrument that is mounted on board the P-3 aircraft, tuned for 10 m above the sea surface, while the Coyote wind observations are direct in situ measurements of the wind at the location of the Coyote sUAS that is typically much higher (~100–600 m). There are also representativeness discrepancies because the Coyote measurements occur at a rate of 1–10 Hz, thus capturing turbulent scales in addition to the mesoscale, while the SFMR foot print of ~2 km does not capture any turbulent scales of air motion.

As for spread ratio, the results are comparable to those observed in Tier A (Fig. 12b) and consistent with their Coyote counterparts shown in Fig. 8 (rows 4 and 6). The reasoning is similar to that discussed in Tier A: although the number of observations assimilated increases as Coyote observations are also assimilated, the increase in the total number of observations is small in a relative sense because the total number of observations is still dominated by the TDR superobs by one order of magnitude (Table 1).

3) TIER C: COYOTE OBSERVATIONS WITH ONLINE QC

When online QC is turned on as the final step, substantial additional improvements are obtained for most observation types and in terms of both total error and spread ratio (Fig. 12, row 3). The largest improvements are for both wind and thermodynamic platforms at the locations of Other observation locations, where improvements are by ~0.8 m s^{-1} (~18%), ~0.5 K (~36%), and ~1 g kg^{-1} (~58%) for wind, temperature, and specific humidity, respectively. These are accompanied by parallel improvements in the spread ratio (by 0.15–0.3). As explained before, these results are not entirely surprising because online QC, by design, eliminates the observations with highest magnitudes of innovations, which leads to a reduction in both total error [through Eqs. (3) and (4)] and spread ratio [both by reducing the total number of observations assimilated and through Eq. (6)].

A closer inspection of where observations filtered out by online QC are located relative to the storm center (Fig. 13) reveals that there is a higher concentration of observations that are eliminated as their distance to the storm center decreases, more so for wind than thermodynamic observations. (Note that the apparent large number of Coyote wind observations filtered out is a plotting artifact that arises from their large spatial density. In actuality, only ~11% of Coyote wind observations are not assimilated, as is shown in Table 1.) Recalling that all observations are processed in a storm-relative framework (Aksoy 2013), it is hypothesized that position errors due to such processing become greater as distance to the storm center decreases. Also, because of their directional component, errors of wind observations are likely to be more sensitive to position uncertainty than their thermodynamic counterparts. A further noteworthy observation is that at the radii of 200–250 km (Figs. 13a,b), there is a significant proportion of the flight-level thermodynamic observations that are filtered out while their wind counterparts passed the online QC.

d. Full impact of Coyote observations in observation space

While it is useful to investigate the impact of frequent cycling and online QC individually and incrementally to understand and improve their effectiveness as optimization tools in data assimilation, it is nevertheless useful to understand the full impact of the Coyote observations with all available optimization options turned on. Figure 14 summarizes these results for observation types, where the improvements shown are now against Control where no Coyote observations are assimilated and no optimization is applied.

For wind observations (Fig. 14a), not surprisingly, the greatest improvements occur at the locations of the Coyote observations themselves: A combination of rms error improvements by ~5 m s^{-1} and bias improvements by ~1.5 m s^{-1} results in total error improvements over ~6.5 m s^{-1}. The spread ratio is also improved by ~0.15. At the locations of the other wind observation types, the impact from assimilating Coyote observations is only indirect. Nevertheless, positive impact is evident for TDR superobs and Other wind observations. For TDR superobs, the improvement by ~1 m s^{-1} is mostly in rms error. Considering that the assimilation of TDR superobs has already been mostly optimized in past studies

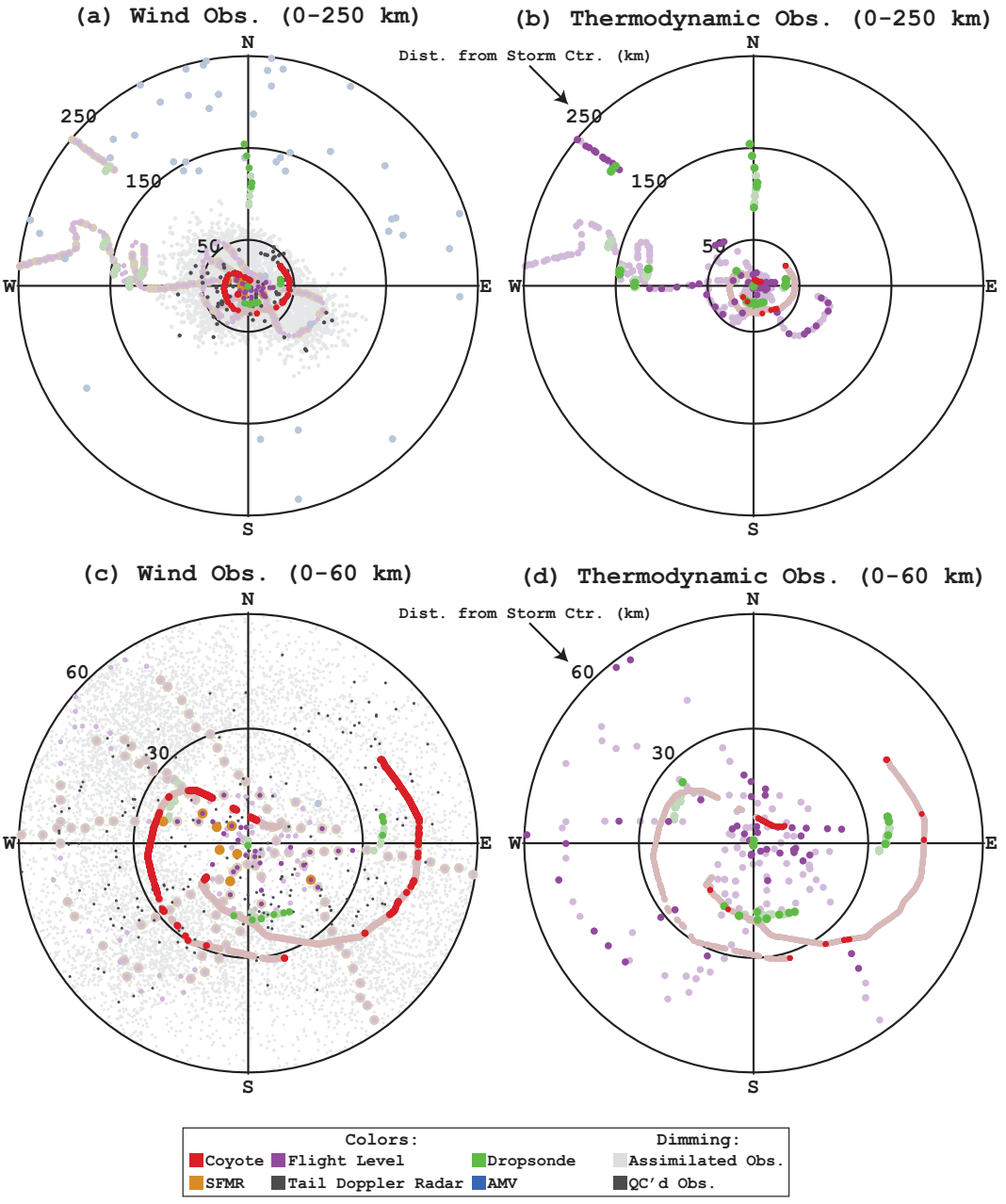

FIG. 13. Locations of observations filtered out by online QC within (a),(b) 250 and (c),(d) 60 km of the storm center: (left) wind observations and (right) thermodynamic observations. The platforms from which observations were obtained are indicated by the marker colors. Observations that were filtered out by online QC are shown in bright (nondimmed) colors. All observations are storm centered, accounting for their horizontal position relative to the storm position interpolated at the time of measurement. (Note that some thinning is applied judiciously to enhance the visibility of observations from various platforms. For a comparison of the actual number of observations, refer to Table 1.)

(e.g., Aksoy et al. 2013), a further improvement of this magnitude is considered an important advancement. Meanwhile, for the Other wind observations, a total improvement of similar magnitude is more evenly distributed between rms error and bias. These improvements are accompanied by parallel improvements in the spread ratio by ~0.1. Finally, for the AMV and SFMR wind speed observation types, the impact of the Coyote observations is negligible in terms of total error. There is also a slight degradation in spread ratio.

For thermodynamic observations (Fig. 14b), more pronounced improvements are obtained. As was the case for the Coyote wind observations, the improvement for Coyote

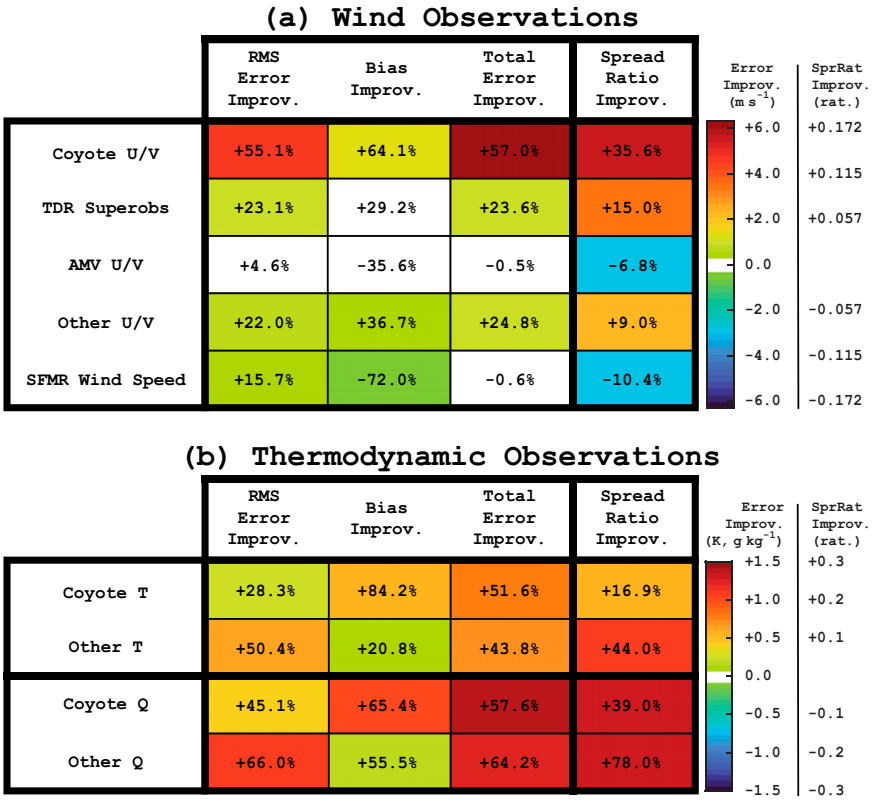

FIG. 14. Average combined impact of frequent cycling (Exp. 3, 25 × 5-min cycles), Coyote observations, and online QC compared to the Control for observation-space diagnostics calculated over all assimilation cycles at the locations of all observation platforms, where "Other" refers to the combined flight-level and dropsonde platforms: (a) wind observations and (b) thermodynamic observations. Positive numbers indicate improvement relative to the Control, while negative numbers indicate degradation. The magnitude-wise change for a given statistic is indicated by the color scale and the corresponding percent change is printed in the respective cell.

temperature (by ~0.8 K, 52%, for total error) and specific humidity (by ~1.4 g kg^{-1}, 58%, for total error) is primarily driven by the fact the Coyote observations were not assimilated in the Control experiment. But unlike the Coyote wind observations, the improvements are mostly in bias rather than rms innovation. As was discussed before, a large part of this is simply due to the lack of a dense set of thermodynamic observations that was already assimilated in the Control experiment. Therefore, Coyote observations provide a major source of thermodynamic information in the inner-core PBL, leading to large reductions in bias through their assimilation. However, the positive impact is not limited to just the Coyote observations. On the contrary, the reduction in total error at the location of Other thermodynamic observations is by nearly the same magnitude or greater both in absolute and relative terms. But unlike the Coyote observations, error reduction is predominantly in terms of rms innovations, likely because bias was already reduced by their assimilation in the Control experiment. Finally, significant improvement in the spread ratio is also obtained for all thermodynamic observations by 0.15–0.3. As was discussed before, this is mainly through the application of online QC.

5. Results in model space

In this final section, the focus turns to the comparison of storm structure in model space. As in the previous section, the focus is on comparing the final analyses obtained in the four experiments, the Control experiment with default cycling strategy (9 × 15-min cycles, Exp. 1) and three further experiments that are based on the Exp. 3 cycling strategy (25 × 5-min cycles): no Coyote observations, with Coyote observations, and with Coyote observations and online QC.

a. *Summary statistics*

Table 3 provides a summary of the observed and analyzed statistics for intensity, MSLP, and storm position. In the analyses obtained in the four experiments mentioned, the intensity is reduced from the highest estimate of 44.7 m s^{-1} in the Control to 38.0 m s^{-1} in the final experiment with 25 × 5-min

TABLE 3. Summary of observed and analyzed intensity and MSLP, as well as position error for the four experiments shown.

	Intensity ($m\ s^{-1}$)	MSLP (hPa)	Position error (km)
Observations (NHC report)[a]	51.4	952	—
Observations (SFMR)[b]	40.5	—	—
Observations (dropsondes)[c]	—	950	—
Experiments			
Control (9 × 15 min)	44.7	944.8	8.4
+ 25 × 5-min cycles (Expt 3)	41.6	947.9	6.2
+ Coyote observations	43.1	948.4	5.9
+ online QC	38.0	949.2	5.9

[a] Pasch et al. (2018), p. 12.
[b] Maximum observed SFMR-retrieved 10-m wind speed within assimilation window, based on dataset obtained from www.aoml.noaa.gov/hrd/Storm_pages/maria2017/20170923H1.html.
[c] Minimum near-surface pressure within assimilation window, as observed by a dropsonde that was released by the NOAA P-3 aircraft at 1917 UTC.

cycles, Coyote observations, and online QC. In similar fashion, MSLP increases from 944.8 hPa in the Control to 949.2 hPa in the final experiment. Finally, position error is reduced from 8.4 km in the Control to 5.9 km in the final experiment. In all these situations, the overestimation of the vortex strength in the Control appears to be reduced with higher-frequency cycling, Coyote observations, and introduction of online QC.

As for the observed intensity and MSLP, according to the official NHC storm report (Pasch et al. 2018), NHC's estimate as of the analysis time of 1800 UTC 23 September 2017 was 51.4 $m\ s^{-1}$ and 952 hPa, respectively. However, as noted in Table 3, these estimates differ from the maximum instrument-observed 10-m wind speed, which was 40.5 $m\ s^{-1}$ that was obtained by the SFMR, while the minimum surface pressure measured by a dropsondes was 950 hPa. These differences and their consequences are discussed further in the summary and discussion section.

b. *Kinematic and thermodynamic structure*

Further investigation of actual model fields reveals important modifications introduced by higher-frequency cycling, Coyote observations, and online QC. Figure 15 shows how the 10-m wind speed field is modified from the Control configuration. The magnitude of the strongest wind speed is gradually reduced as its location is pushed outward from a radius of ~30 km in the Control (Fig. 15a) to ~50 km in the final experiment (Fig. 15d).

The three-dimensional wind structure is further investigated in an azimuthally averaged sense by plotting the tangential (Fig. 16), radial (Fig. 17), and vertical (Fig. 18) components of the wind. Also known as the primary circulation, the tangential wind speed undergoes noteworthy changes as experiments progress. To focus on the boundary layer where the biggest differences are present among the experiments, only the boundary layer structure within 0–2-km height is shown. Without the Coyote observations (Figs. 16a,b), the strongest winds are confined inside 50 km and maximized at a radius of ~37 km. The addition of the Coyote observations (Fig. 16c) results in both the strengthening of the primary circulation and the expansion of the strongest wind speed to a radius of ~70 km. Online QC results in further significant modification by weakening the circulation by ~2–3 $m\ s^{-1}$.

The radial wind speed (i.e., the horizontal component of the secondary circulation) reflects changes in structure that are consistent with the primary circulation (Fig. 17). The boundary layer height is depicted by the 10% maximum radial inflow contour as in Zhang et al. (2011, see their Fig. 5). The strongest part of the inflow (negative wind speed) expands from a radius of ~30–40 km without the Coyote observations to ~70 km with them. Meanwhile, although a low-level outflow jet exists in the Control experiments (Figs. 17a,b), its radial location is at ~75 km, which is not consistent with the location of the outflow jet that is typically observed near the radius of maximum wind (Zhang et al. 2011). With Coyote observations (Fig. 17c), this structure becomes more self-consistent as the outflow jet is pushed inward to ~60 km. Application of online QC (Fig. 17d) further eliminates the stronger part of the outflow jet inside 50 km. Overall, a much more consistent radial inflow structure is obtained as Coyote observations are assimilated and then online QC is applied.

There are also significant changes in the vertical part of the secondary circulation (i.e., azimuthally averaged vertical wind speed, Fig. 18). Since the vertical wind speed spans a greater range in height, variations across most of the troposphere are shown between 0 and 14 km. Again, in the Control experiments (Figs. 18a,b), the radial location of the strongest upward motion is inside 50 km. Assimilating the Coyote observations (Figs. 18c,d) modifies this structure and results in a more-enhanced updraft region outside 50 km and weakens the inner updraft region significantly.

Finally, the thermal structure is evaluated through the azimuthally averaged temperature perturbation relative to the storm environment at 500-km radius (Fig. 19). First, there appears to be a weakening of the warm core by ~0.5°–1°C from the Control (Figs. 19a,b) to Coyote (Figs. 19c,d) experiments, which is consistent with the overall weakening of the wind field discussed before. There is also a slight warming near the radius of ~100 km near the height of 8 km. Within the PBL and especially near the ocean surface (inserts in each panel), the strongest part of the precipitation-induced cooling moves inward from outside of the radius of 100 km in the Control experiments (Figs. 19a,b) to a radius of 50–100 km in the Coyote experiments (Figs. 19c,d). This shift is more consistent with the location of the stronger updraft region at similar radii that is observed in the same experiments (Figs. 18c,d).

c. *Comparison to observed storm structure*

Since almost all available TC inner-core in situ observations are assimilated in HEDAS, it is generally challenging to compare HEDAS storm-scale analyses to independent observations. The one exception is the TDR reflectivity that is not assimilated due to known biases that exist in the measurements. Figure 20 provides a comparison of the analyzed

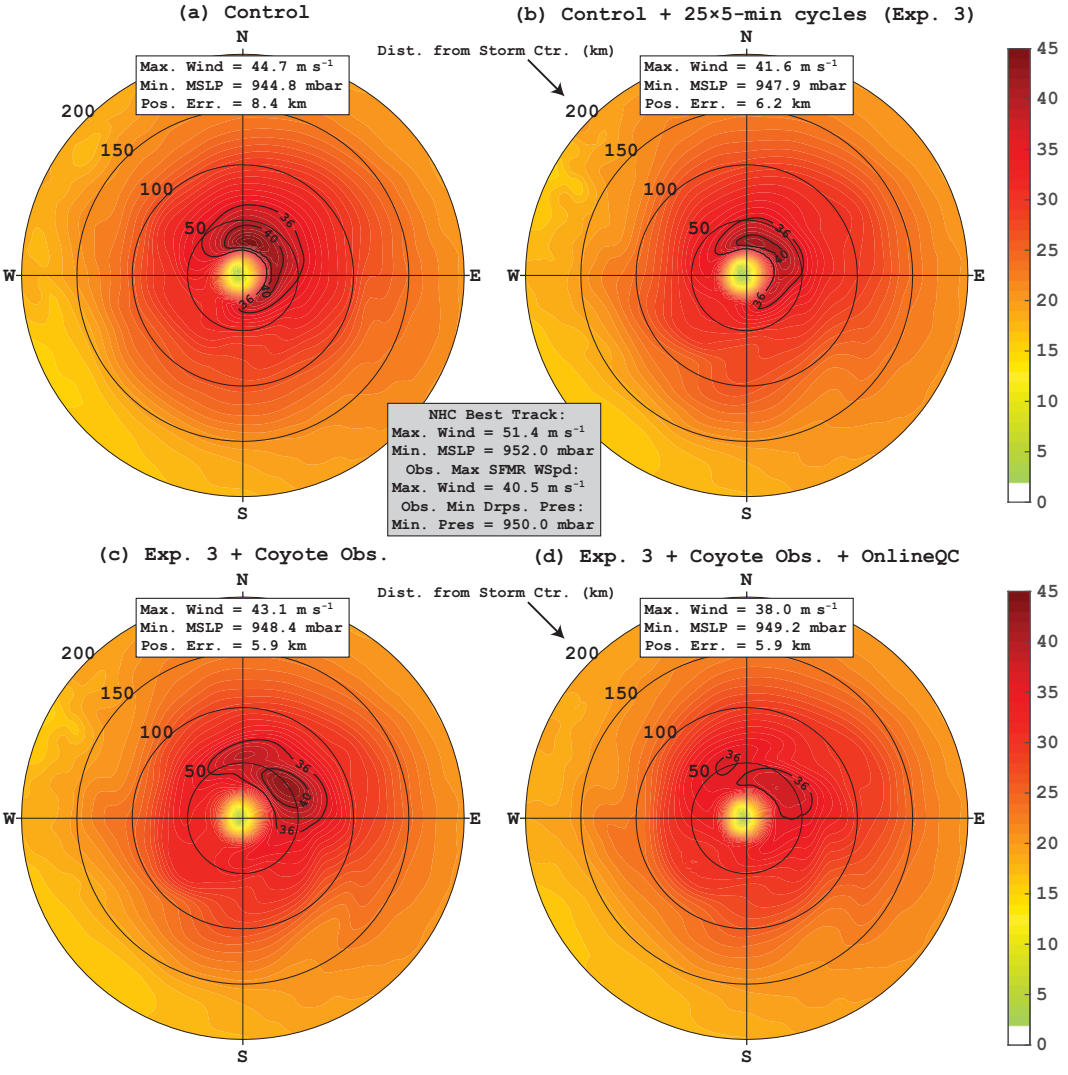

FIG. 15. Storm-relative plan view of 10-m wind speed (m s^{-1}) from the final analyses in the following experiments: (a) Control; (b) Control with frequent cycling (Exp. 3, 25 × 5-min cycles); (c) Control with frequent cycling (Exp. 3, 25 × 5-min cycles) and Coyote observations; and (d) Control with frequent cycling (Exp. 3, 25 × 5-min cycles), Coyote observations, and online QC. Black contours indicate the area of stronger wind speeds. Corresponding maximum wind speed, minimum sea level pressure, and position error are printed in white boxes. Estimates of intensity and MSLP based on NHC best track data as well as observed maximum SFMR wind speed are shown in the gray box in the center.

and composite observed TDR reflectivity and horizontal wind speed at 2-km height. In a qualitative sense, the corresponding analyzed and observed fields correspond well to each other. An inner reflectivity maximum at ~25-km radius appears both in analyzed and observed fields (Figs. 20a,b). However, although a localized wind speed maximum is discernable at the same location in the corresponding observed wind speed field (Fig. 20d), no corresponding maximum exists its analyzed counterpart (Fig. 20c).

Meanwhile, the high-wind speed region at ~50–60-km radius and the associated wavenumber-1 asymmetry correspond to each other very well in the analysis and observations (Figs. 20c,d), although the highest wind speed in the northeast quadrant is slightly overestimated in the analysis compared to the TDR observations. Finally, the primary rainband is more pronounced in the analysis north of the center and extends further out radially in the southeast quadrant compared to the observations. Despite some differences, it is generally concluded that there is a very good agreement between the observed and analyzed structures of reflectivity and horizontal wind speed near the inner core.

6. Summary and discussion

A unique dataset obtained from the Coyote small uncrewed aircraft system (sUAS) in the inner-core planetary boundary

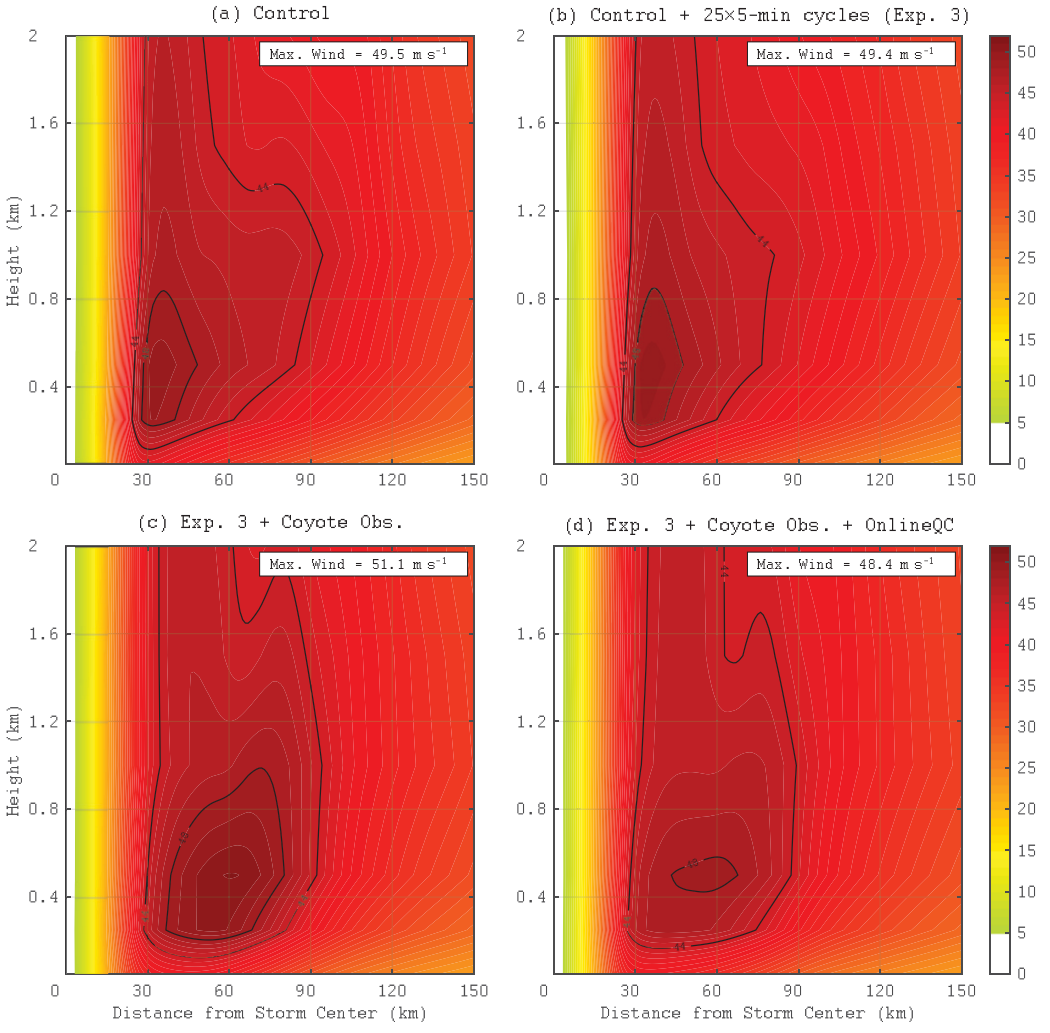

FIG. 16. As in Fig. 15, but for the radial–height view of tangential wind speed (m s^{-1}) at heights 0–2 km. Corresponding maximum wind speed is printed in boxes.

layer (PBL) of Hurricane Maria (2017) is assimilated using NOAA's Hurricane Ensemble Data Assimilation System (HEDAS) and the forecast model part of NOAA's Hurricane Weather Research and Forecasting (HWRF) system. The data assimilated in HEDAS for this case comprise observations collected by the NOAA Lockheed WP-3D Orion (P-3) and U.S. Air Force C-130 (C-130) aircraft. Additionally, atmospheric motion vector (AMV) wind observations were assimilated. The unique aspect about this case is that two Coyote sUAS platforms were flown in the eyewall PBL that collected and relayed back to the P-3 in situ observations of horizontal wind, temperature, relative humidity, and atmospheric pressure.

A new online quality control (QC) technique is developed in HEDAS to support the assimilation of this unique dataset described above. This is in addition to the traditional QC step that occurs during the preprocessing of observations and takes advantage of the knowledge of model background information during assimilation, hence the term "online." Assimilation experiments are carried out for four cycling scenarios, ranging from the default of 15-min cycling intervals to 5 min. Further experiments are conducted at each cycling scenario with a Control that does not assimilate Coyote observations, assimilation of Coyote observations in addition to the Control observations, and the application of online QC.

In the following, a point-by-point summary of the findings of the study is provided:

- At the locations of the Coyote observations, higher-frequency cycling slightly improves the wind bias and almost completely eliminates the temperature and specific humidity bias in the Control experiments. Since thermodynamic observations are likely impacted more by smaller-scale processes such as convection, higher-frequency cycling is believed to lead to larger improvements in bias by resulting in more-linear updates and smaller innovations as a consequence.

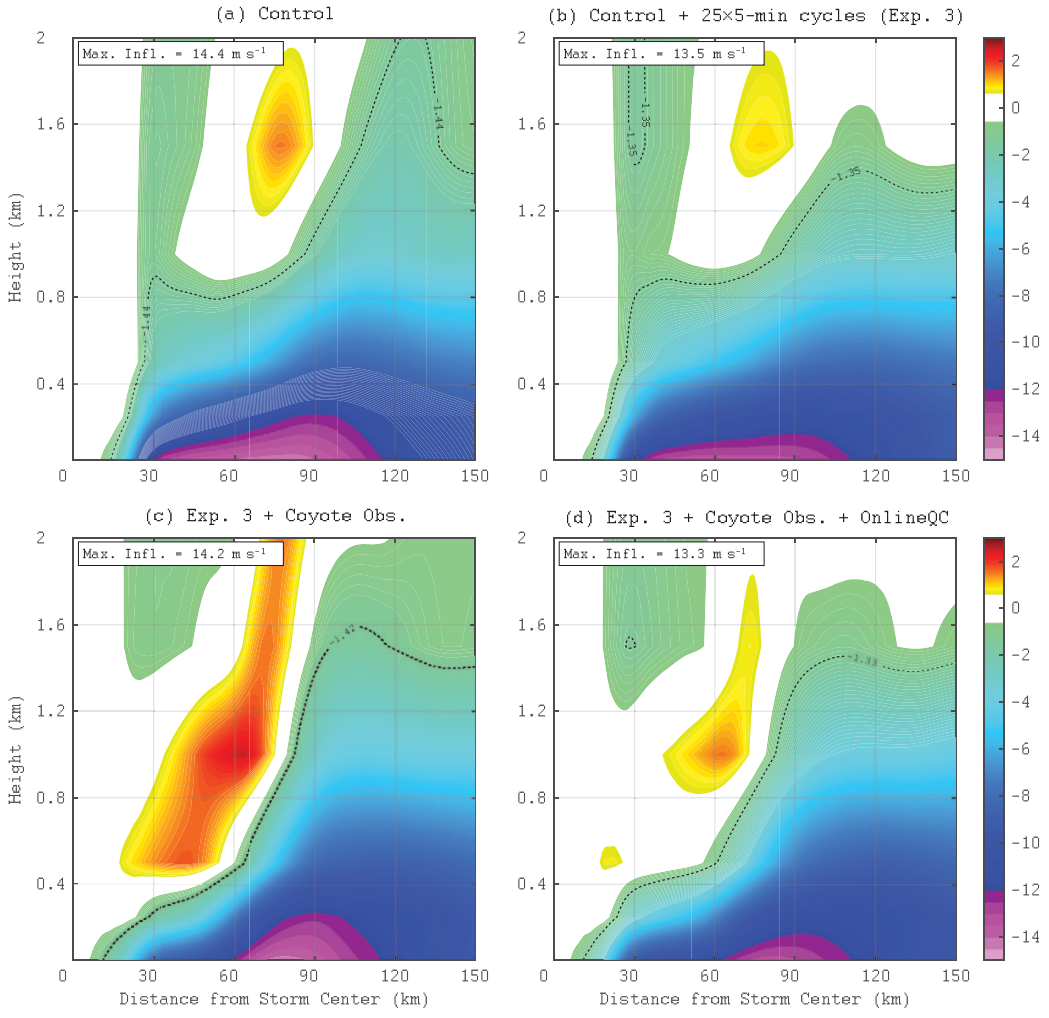

FIG. 17. As in Fig. 16, but for radial wind speed (m s^{-1}). Inflow is depicted in negative contours and outflow is depicted in positive contours. The dashed black lines indicate the height where the radial wind speed is 10% of the peak inflow.

- When Coyote observations are assimilated, errors for both the wind and thermodynamic observations are significantly reduced at the locations of the Coyote observations. The addition of higher-frequency cycling introduces further improvements, but mostly for the Coyote wind observations.
- The final step of additional online QC introduces large improvements in ensemble spread and modest improvements in total error for all Coyote observations. This is both a direct result of filtering out observations with largest departures from the model background but also an indirect result of more-linear filter updates achieved through the elimination of such departures. One confirmation of this hypothesis is obtained from the fact that fewer observations, especially Coyote wind observations, are filtered out by online QC in the experiments with more-frequent cycling as a result of more-linear updates with smaller innovations.
- The impact of higher-frequency cycling, Coyote assimilation, and online QC at the locations of non-Coyote observations is also mostly positive. Although Coyote assimilation itself only results in small changes in the total error, both higher-frequency cycling and online QC result in large improvements both for wind (mostly observed at TDR, flight-level, and dropsonde locations) and thermodynamic (observed at all locations) observations. Large spread-ratio improvements are also obtained for thermodynamic observations.
- The combined total impact of Coyote assimilation, high-frequency cycling, and online QC is generally positive for all observation types. At the locations of Coyote observations, total wind, temperature, and specific humidity errors are reduced by ~6 m s^{-1} (57%), 0.8 K (52%), and 1.4 g kg^{-1} (58%), respectively. At the locations of TDR, flight-level, and dropsonde wind observations, wind error is improved by ~1 m s^{-1} (24%). At the locations of non-Coyote temperature and specific humidity observations, total error is reduced by 0.7 K (44%) and 1.2 g kg^{-1} (64%), respectively. All of these reductions in error are also accompanied by

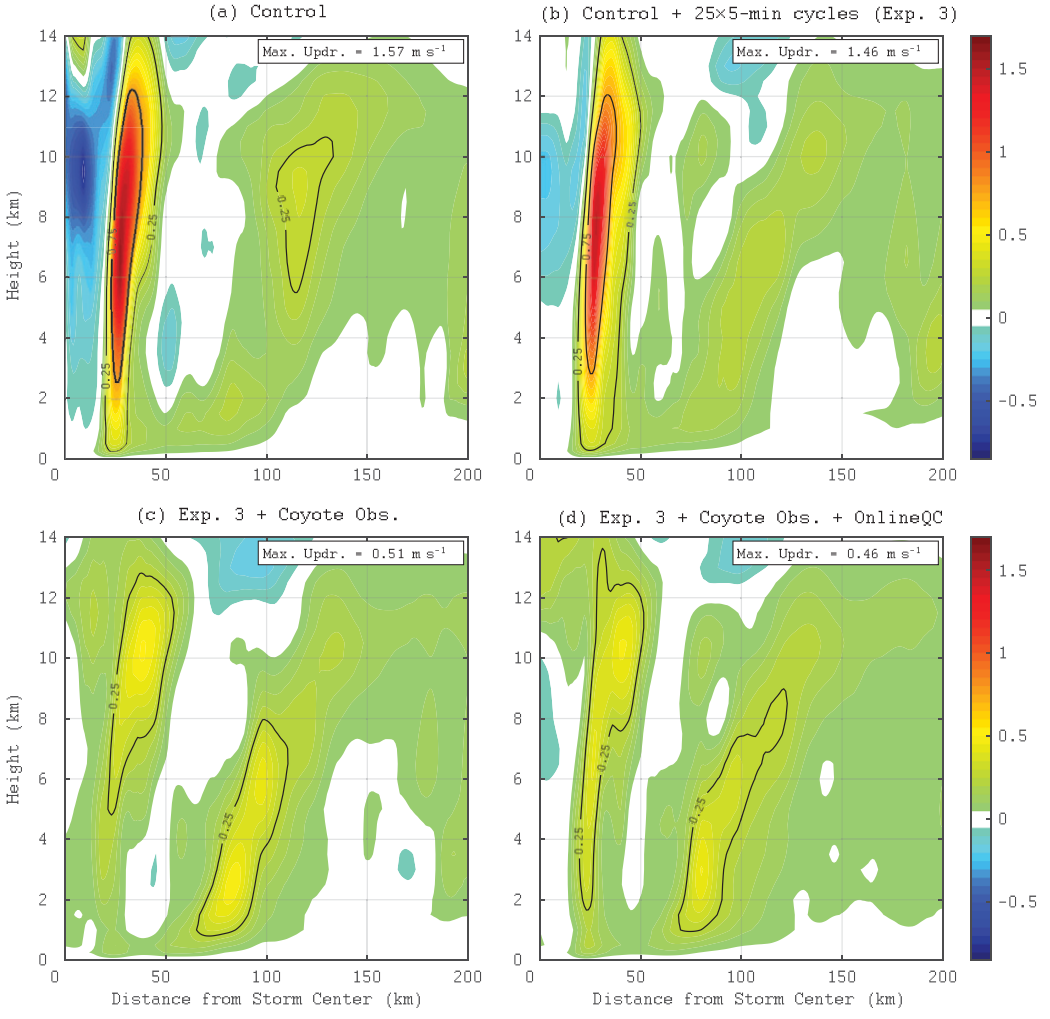

FIG. 18. As in Fig. 16, but for vertical wind speed (m s^{-1}) at heights 0–14 km.

parallel improvements in spread ratio in a generally proportional sense.

- Finally, a comparison of the final analyses in model space reveals important modifications to the storm structure by frequent cycling, Coyote observations, and online QC. The most important impact is in the ability of the Coyote observations to introduce the more-prominent wider eyewall feature that is otherwise not reproduced well in any of the Control experiments, even with high-frequency cycling. Further application of online QC maintains the wide eyewall structure but reduces storm intensity to better match observations. These modifications appear to be present and consistent in all aspects of storm structure, including near-surface, tangential, radial, and vertical wind speed as well as temperature perturbation.

As a general summary, it is concluded that, for effective DA, it is crucial not only to observe in more detail the inner-core PBL of TCs but also to modify data assimilation methodology to make better use of those observations. In the particular case presented in this study, data from the two Coyote sUAS flights were able to modify the resulting analyzed storm structure significantly. However, further application of frequent cycling and online QC was needed to better match the observed storm intensity and MSLP.

It is also noteworthy that both frequent cycling and online QC in essence work to reduce the nonlinearities in the application of DA. The former achieves this by reducing the departures in the background fields from observations through shorter model advances in-between DA cycles while the latter helps by eliminating large observation-background departures through the comparison of normalized innovations among all observations. Regardless of methodology, it is important to acknowledge the limitations of ensemble Kalman filter (EnKF) DA techniques in highly nonlinear applications such as in the TC inner core. Although the results presented here indirectly speak to the need of further research in nonlinear DA applications, it is equally critical to acknowledge the importance of high-frequency observations that can support further linearization efforts in traditional EnKF methods.

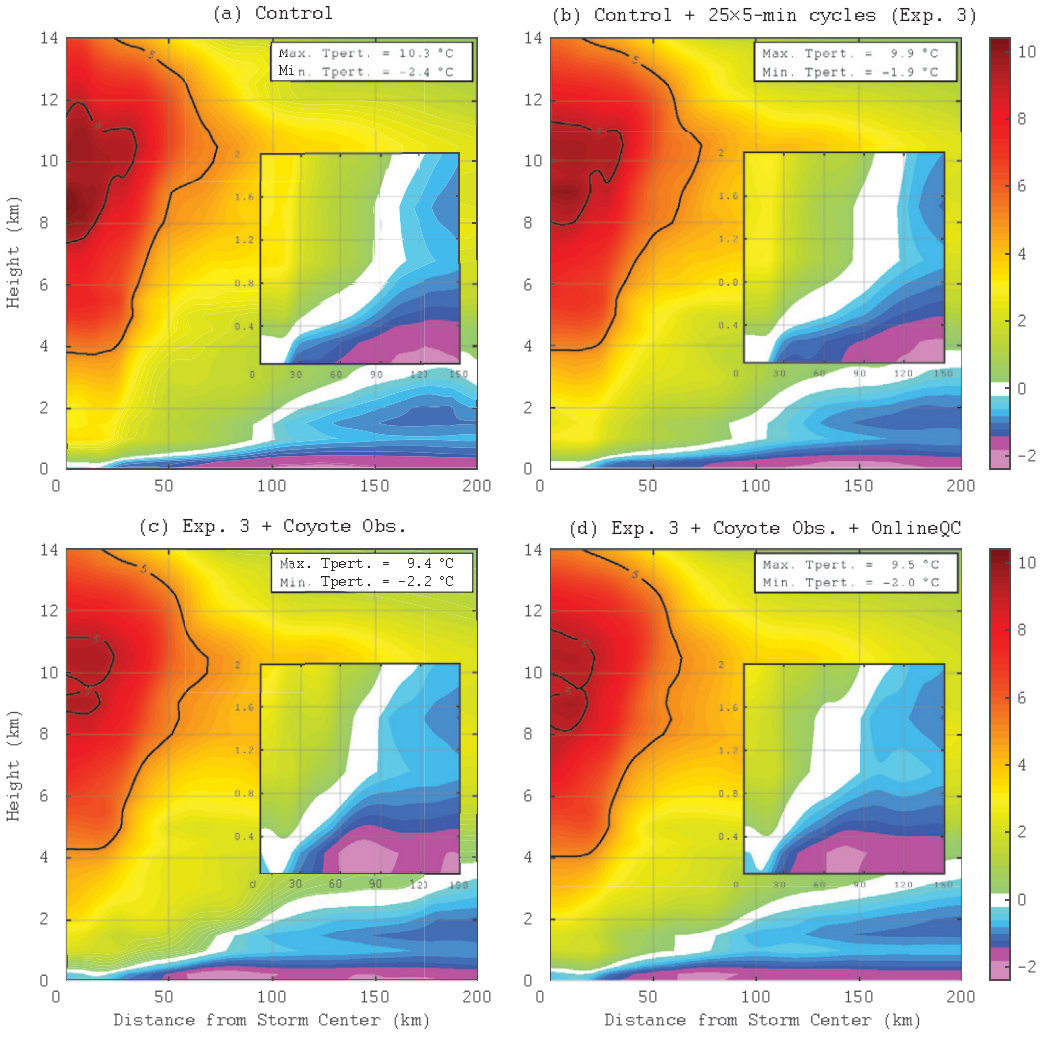

FIG. 19. As in Fig. 16, but for temperature perturbation (°C) at heights 0–14 km. Inserts in each panel show a close-up view in the PBL between heights 0–2 km and radii 0–150 km.

A further issue is related to how best to verify intensity and MSLP. Traditionally, this is done by comparing the highest 10-m wind speed and minimum sea level pressure found in the analysis output to what is reported in NHC's best track dataset. In the present case, however, there are significant differences between metrics calculated from analysis fields and those reported in the best track. Specifically, observed MSLP as reported by the best track is 952 hPa while those in the analyses vary between 945 and 949 hPa. Even more strikingly, although the observed best track intensity is 51.4 m s^{-1}, analyzed intensity appears significantly underestimated and remains in the range of 38.0–44.7 m s^{-1}. However, when directly compared to the actual lowest pressure and highest 10-m wind speed measured by any instrument within the 6-h analysis window, the analyzed intensity and MSLP appear much closer to observed. The lowest MSLP observed by the dropsondes near the storm center is 950 hPa and the highest wind speed observed by the SFMR is 40.5 m s^{-1}. It is important to note that data assimilation is an objective procedure that can only reflect the additional information content of the observations that it assimilates. Meanwhile, the NHC best track is a human-generated dataset where subjective considerations beyond just the available observations frequently impact the final estimates of intensity and MSLP. Therefore, caution must be exercised when verifying analysis intensity and MSLP by investigating all available sources of information to decide their representativeness in a given case.

It should also be noted here that the main strength of the Coyote (or any other sUAS) platform is the ability to guide it into a region of interest and sample it at high frequency with standard in situ sensors. Similar sampling capability would not be possible with dropsonde observations as they cannot be steered once released from aircraft, nor with crewed-aircraft-mounted sensors because it is prohibitively dangerous to fly in these regions. This strength is expected to become even more amplified in the near future as technology advances

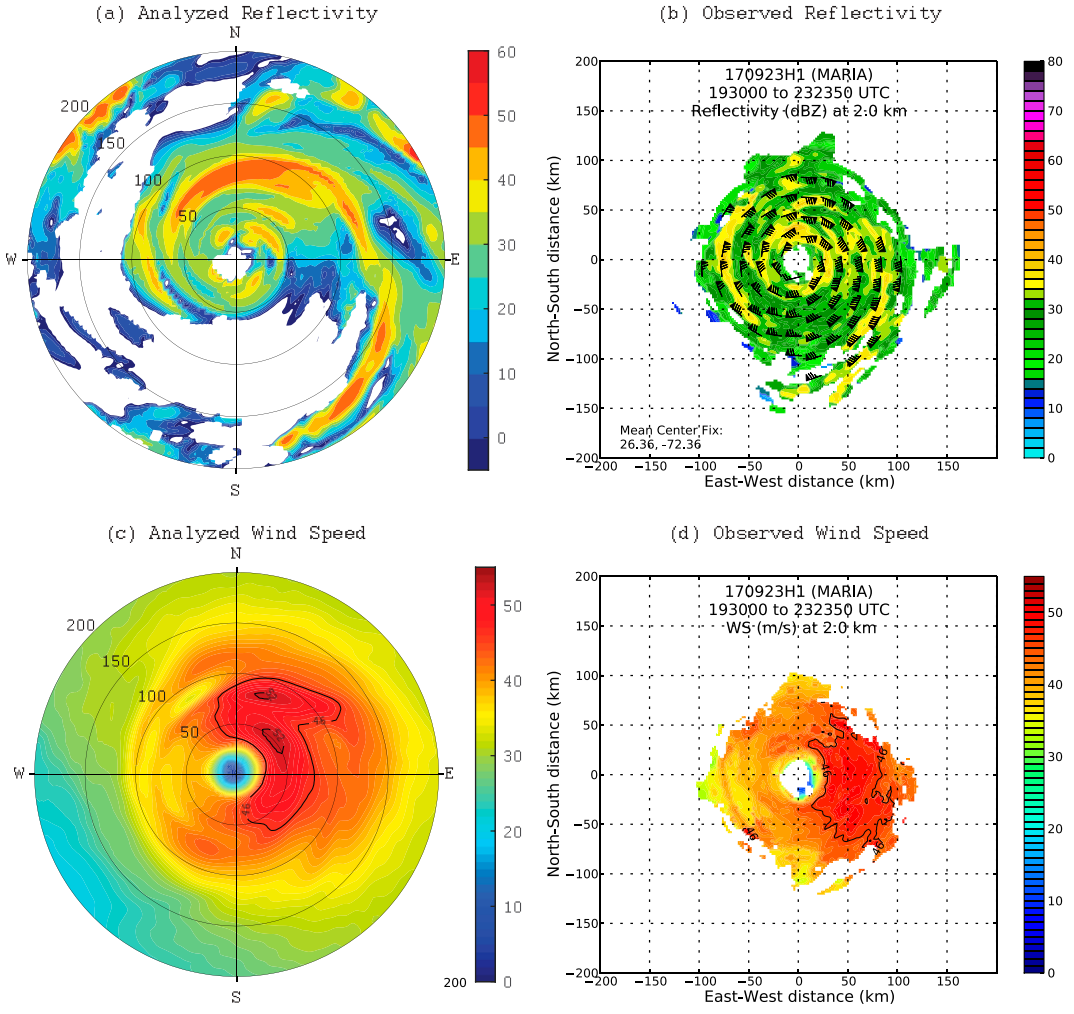

FIG. 20. Comparison of (left) analyzed fields (Exp. 3 + Coyote obs. + Online QC) to (right) observed fields at 2-km height. Reflectivity is shown on the top and horizontal wind speed (m s^{-1}) is shown on the bottom. All fields are plotted in storm-relative coordinates.

allow sUAS to remain airborne for longer time periods (upward of 4 h compared to the Coyote's nominal 1-h battery life), guide themselves according to specified meteorological criteria using advanced artificial intelligence technology, and/or be guided in real time from the crewed aircraft using more advanced technology that allows two-way communication at longer distances.

Finally, it is important to acknowledge some of the limitations of the present study to place the results in better context. First, the results are based on a single case, which obviously limits their interpretation in a general sense. Nevertheless, despite the significant number of variations in experimental setup, the variability among the results was mostly constrained to where and how observations were assimilated. The authors believe that this is an indication of stability in their findings and expect that their conclusions must apply to similar scenarios equally well. It is also important to note that only focusing on DA results is expected to minimize the impact of model error that otherwise should introduce a much greater variability among experiments if forecasts were also included in the investigation. To generalize the validity of the results presented here, the authors plan to expand their study to all of the cases that include Coyote (and planned future sUAS) observations, which will be reported in the near future in a separate study. A parallel study is also underway to investigate how assimilation of the Coyote observations impacts NOAA's operational forecasts.

Acknowledgments. Partial funding support was provided through the Cooperative Agreement NA67RJ0149 between NOAA and the University of Miami. Appreciation goes out to all NOAA Aircraft Operations Center (AOC) staff who supported P-3 sUAS Hurricane Hunter missions into Maria (2017). Without their dedication these missions would not have been possible. The authors acknowledge the NOAA Research and Development High Performance Computing

Program for providing computing and storage resources that have contributed to the research results reported within this paper (https://rdhpcs.noaa.gov). Kathryn Sellwood (University of Miami/CIMAS and NOAA/AOML/HRD) was instrumental with the preprocessing of observations assimilated. Internal reviews by Sean Casey (University of Miami/CIMAS and NOAA/AOML/HRD) and Jason Sippel (NOAA/AOML/HRD) greatly enhanced the quality of the manuscript. The authors also thank three anonymous reviewers who provided excellent comments that improved the manuscript.

Data availability statement. All raw observations for Hurricane Maria (2017) are available through the NOAA/AOML/HRD data portal at https://www.aoml.noaa.gov/hrd/Storm_pages/maria2017. Further postprocessed datasets are available directly from the authors upon request.

REFERENCES

Aberson, S. D., A. Aksoy, K. J. Sellwood, T. Vukicevic, and X. Zhang, 2015: Assimilation of high-resolution tropical cyclone observations with an ensemble Kalman filter using HEDAS: Evaluation of 2008–11 HWRF forecasts. *Mon. Wea. Rev.*, **143**, 511–523, https://doi.org/10.1175/MWR-D-14-00138.1.

Aksoy, A., 2013: Storm-relative observations in tropical cyclone data assimilation with an ensemble Kalman filter. *Mon. Wea. Rev.*, **141**, 506–522, https://doi.org/10.1175/MWR-D-12-00094.1.

——, D. C. Dowell, and C. Snyder, 2009: A multicase comparative assessment of the ensemble Kalman filter for assimilation of radar observations. Part I: Storm-scale analyses. *Mon. Wea. Rev.*, **137**, 1805–1824, https://doi.org/10.1175/2008MWR2691.1.

——, S. Lorsolo, T. Vukicevic, K. J. Sellwood, S. Lorsolo, S. D. Aberson, and F. Zhang, 2012: The HWRF Hurricane Ensemble Data Assimilation System (HEDAS) for high-resolution data: The impact of airborne Doppler radar observations in an OSSE. *Mon. Wea. Rev.*, **140**, 1843–1862, https://doi.org/10.1175/MWR-D-11-00212.1.

——, S. D. Aberson, T. Vukicevic, K. J. Sellwood, S. Lorsolo, and X. Zhang, 2013: Assimilation of high-resolution tropical cyclone observations with an ensemble Kalman filter using NOAA/AOML/HRD's HEDAS: Evaluation of the 2008–11 vortex-scale analyses. *Mon. Wea. Rev.*, **141**, 1842–1865, https://doi.org/10.1175/MWR-D-12-00194.1.

Auligné, T., and A. P. McNally, 2007: Interaction between bias correction and quality control. *Quart. J. Roy. Meteor. Soc.*, **133**, 643–653, https://doi.org/10.1002/qj.57.

Bannister, R. N., 2017: A review of operational methods of variational and ensemble-variational data assimilation. *Quart. J. Roy. Meteor. Soc.*, **143**, 607–633, https://doi.org/10.1002/qj.2982.

Bauer, P., A. Thorpe, and G. Brunet, 2015: The quiet revolution of numerical weather prediction. *Nature*, **525**, 47–55, https://doi.org/10.1038/nature14956.

Ben-Gal, I., 2010: Outlier detection. *Data Mining and Knowledge Discovery Handbook: A Complete Guide for Practitioners and Researchers*, O. Maimon and L. Rokach, Eds., Springer, 117–130.

Bernardet, L., and Coauthors, 2015: Community support and transition of research to operations for the Hurricane Weather Research and Forecasting Model. *Bull. Amer. Meteor. Soc.*, **96**, 953–960, https://doi.org/10.1175/BAMS-D-13-00093.1.

Braun, S. A., and Coauthors, 2013: NASA's Genesis and Rapid Intensification Processes (GRIP) field experiment. *Bull. Amer. Meteor. Soc.*, **94**, 345–363, https://doi.org/10.1175/BAMS-D-11-00232.1.

Christophersen, H., A. Aksoy, J. Dunion, and K. Sellwood, 2017: The impact of NASA Global Hawk unmanned aircraft dropwindsonde observations on tropical cyclone track, intensity, and structure: Case studies. *Mon. Wea. Rev.*, **145**, 1817–1830, https://doi.org/10.1175/MWR-D-16-0332.1.

——, ——, ——, and S. Aberson, 2018a: Composite impact of Global Hawk unmanned aircraft dropwindsondes on tropical cyclone analyses and forecasts. *Mon. Wea. Rev.*, **146**, 2297–2314, https://doi.org/10.1175/MWR-D-17-0304.1.

——, R. Atlas, A. Aksoy, and J. Dunion, 2018b: Combined use of satellite observations and Global Hawk unmanned aircraft dropwindsondes for improved tropical cyclone analyses and forecasts. *Wea. Forecasting*, **33**, 1021–1031, https://doi.org/10.1175/WAF-D-17-0167.1.

Cione, J. J., E. A. Kalina, E. W. Uhlhorn, A. M. Farber, and B. Damiano, 2016: Coyote unmanned aircraft system observations in Hurricane Edouard. *Earth Space Sci.*, **3**, 370–380, https://doi.org/10.1002/2016EA000187.

——, and Coauthors, 2020: Eye of the storm: Observing hurricanes with a small unmanned aircraft system. *Bull. Amer. Meteor. Soc.*, **101**, E186–E205, https://doi.org/10.1175/BAMS-D-19-0169.1.

He, H., L. Lei, J. S. Whitaker, and Z.-M. Tan, 2020: Impacts of assimilation frequency on ensemble Kalman filter data assimilation and imbalances. *J. Adv. Model. Earth Syst.*, **12**, e2020MS002187, https://doi.org/10.1029/2020MS002187.

Hock, T. F., and J. L. Franklin, 1999: The NCAR GPS dropsonde. *Bull. Amer. Meteor. Soc.*, **80**, 407–420, https://doi.org/10.1175/1520-0477(1999)080<0407:TNGD>2.0.CO;2.

Houtekamer, P. L., and F. Zhang, 2016: Review of the ensemble Kalman filter for atmospheric data assimilation. *Mon. Wea. Rev.*, **144**, 4489–4532, https://doi.org/10.1175/MWR-D-15-0440.1.

National Hurricane Center, 2017: National Hurricane Center Forecast Verification. Accessed 3 March 2021, http://www.nhc.noaa.gov/verification.

National Research Council, 1991: Quality control and validation of observations, analyses, and models. *Four-Dimensional Model Assimilation of Data: A Strategy for the Earth System Sciences*, The National Academies Press, 48–50.

Pasch, R. J., A. B. Penny, and R. Berg, 2018: Hurricane Maria (16–30 September 2017). National Hurricane Center Tropical Cyclone Rep. AL152017, 48 pp., https://www.nhc.noaa.gov/data/tcr/AL152017_Maria.pdf.

Poterjoy, A., and F. Zhang, 2011: Dynamics and structure of forecast error covariance in the core of a developing Hurricane. *J. Atmos. Sci.*, **68**, 1586–1606, https://doi.org/10.1175/2011JAS3681.1.

Rogers, R., and Coauthors, 2013: NOAA'S Hurricane Intensity Forecasting Experiment: A progress report. *Bull. Amer. Meteor. Soc.*, **94**, 859–882, https://doi.org/10.1175/BAMS-D-12-00089.1.

Sakov, P., and P. Sandery, 2017: An adaptive quality control procedure for data assimilation. *Tellus*, **69A**, 1318031, https://doi.org/10.1080/16000870.2017.1318031.

Tomassini, L., P. R. Field, R. Honnert, S. Malardel, R. McTaggart-Cowan, K. Saitou, A. T. Noda, and A. Seifert, 2017: The "Grey Zone" cold air outbreak global model intercomparison: A cross evaluation using large-eddy simulations. *J. Adv. Model. Earth Syst.*, **9**, 39–64, https://doi.org/10.1002/2016MS000822.

Tukey, J. W., 1977: *Exploratory Data Analysis.* Addison-Wesley, 688 pp.

Uhlhorn, E. W., P. G. Black, J. L. Franklin, M. Goodberlet, J. Carswell, and A. S. Goldstein, 2007: Hurricane surface wind measurements from an operational stepped frequency microwave radiometer. *Mon. Wea. Rev.*, **135**, 3070–3085, https://doi.org/10.1175/MWR3454.1.

Van Leeuwen, P. J., H. R. Künsch, L. Nerger, R. Potthast, and S. Reich, 2019: Particle filters for high-dimensional geoscience applications: A review. *Quart. J. Roy. Meteor. Soc.*, **145**, 2335–2365, https://doi.org/10.1002/qj.3551.

Velden, C. S., and Coauthors, 2005: Recent innovations in deriving tropospheric winds from meteorological satellites. *Bull. Amer. Meteor. Soc.*, **86**, 205–224, https://doi.org/10.1175/BAMS-86-2-205.

Whitaker, J. S., and T. M. Hamill, 2002: Ensemble data assimilation without perturbed observations. *Mon. Wea. Rev.*, **130**, 1913–1924, https://doi.org/10.1175/1520-0493(2002)130<1913:EDAWPO>2.0.CO;2.

Yano, J.-I., and Coauthors, 2018: Scientific challenges of convective-scale numerical weather prediction. *Bull. Amer. Meteor. Soc.*, **99**, 699–710, https://doi.org/10.1175/BAMS-D-17-0125.1.

Zhang, F., M. Minamide, and E. E. Clothiaux, 2016: Potential impacts of assimilating all-sky infrared satellite radiances from GOES-R on convection-permitting analysis and prediction of tropical cyclones. *Geophys. Res. Lett.*, **43**, 2954–2963, https://doi.org/10.1002/2016GL068468.

Zhang, J. A., R. F. Rogers, D. S. Nolan, and F. D. Marks Jr., 2011: On the characteristic height scale of the Hurricane boundary layer. *Mon. Wea. Rev.*, **139**, 2523–2535, https://doi.org/10.1175/MWR-D-10-05017.1.